Space weathering, grain size, and metamorphic heating effects on ordinary chondrite spectral reflectance parameters

MacLennan, Eric M.

Wiley Blackwell
2024-06

MacLennan, E M, Emery, J P, Lucas, M P, McClure, L M & Lindsay, S S 2024, 'Space weathering, grain size, and metamorphic heating effects on ordinary chondrite spectral reflectance parameters', Meteoritics and Planetary Science, vol. 59, no. 6, pp. 1329-1352. https://doi.org/10.1111/ma

http://hdl.handle.net/10138/576801
10.1111/maps.14150

The Meteoritical Society

Meteoritics & Planetary Science 59, Nr 6, 1329–1352 (2024)
doi: 10.1111/maps.14150

Space weathering, grain size, and metamorphic heating effects on ordinary chondrite spectral reflectance parameters

Eric M. MacLENNAN[1,2]*, Joshua P. EMERY[2,3], Michael P. LUCAS[2], Lucas M. McCLURE[3,4], and Sean S. LINDSAY[2,4]

[1]Department of Physics, University of Helsinki, Helsinki, Finland
[2]Earth and Planetary Sciences Department, Planetary Geosciences Institute, The University of Tennessee, Knoxville, Tennessee, USA
[3]Department of Astronomy and Planetary Science, Northern Arizona University, Flagstaff, Arizona, USA
[4]Department of Physics and Astronomy, The University of Tennessee, Knoxville, Tennessee, USA
*Correspondence
Eric M. MacLennan, Department of Physics, University of Helsinki, PO Box 64, Helsinki 00014, Finland.
Email: eric.maclennan@helsinki.fi

(*Received 20 April 2023; revision accepted 05 February 2024*)

Abstract–The exposure to irradiation from high-energy particles alters the reflectance properties of asteroid surfaces and is referred to as *space weathering*. This process leads to an increase in spectral slope in visible and near-infrared wavelengths. However, changes in the regolith particle size, which can vary dramatically among the asteroid population, are known to influence the spectral properties of meteorites and asteroids. In this context, we investigate the changes in spectral slope and absorption band depths of fresh and irradiated ordinary chondrite meteorites to quantitatively compare the effects of space weathering and grain size variations. To do so, we develop and employ the Spectral Analysis for Asteroid Reflectance Investigation routine that calculates the band parameters of reflectance spectra. We then formulate a parameter called the Space Weathering Index (*SWI*) that is designed to encapsulate spectral changes due to space weathering. We find that the *SWI* is strongly dependent on the spectral slope which complicates the interpretation of asteroid spectra in the context of grain size variations and space weathering. We also show that a second parameter, the Band Depth Index, is indicative of petrologic type. Finally, we use a linear discriminant analysis to classify asteroid reflectance spectra into H, L, LL, and unequilibrated ordinary chondrites.

INTRODUCTION

The term *space weathering* refers to the irradiation of high-energy particles (solar wind ions and micrometeoroids) and the associated spectral changes seen among airless solar system bodies (Hapke, 2001; Pieters & Noble, 2016). The concept of space weathering emerged after the Apollo missions showed differences between samples of the lunar rocks and the fine-grained regolith (e.g., Conel & Nash, 1970; McCord & Johnson, 1970). The combination of petrographic analysis of lunar samples and remote sensing of the lunar surface led to the finding that asteroids are subjected to the same process with similar effects (Brunetto et al., 2015; Pieters et al., 2000; Taylor et al., 2001). The "lunar style" of space weathering is characterized by darkening, spectral reddening, and a decreasing absorption band strength (Adams & McCord, 1971), which can qualitatively explain the differences between fresh meteorite and weathered asteroid spectra among S-complex asteroids (Chapman, 2004).

In addition to space weathering, grain size is another non-compositional characteristic that influences the spectral slope and band depth (Adams & Filice, 1967; Hasegawa et al., 2019). Many studies have shown that grain size estimates vary over many orders of magnitude in the asteroid population (Delbo & Tanga, 2009; Delbo et al., 2007; Gundlach & Blum, 2013; MacLennan & Emery, 2022; Vernazza et al., 2016). It is clear that this

variation is partly influenced by asteroid size, which can lead to possible misinterpretation of spectral trends in the context of space weathering.

The ordinary chondrite meteorites have undergone different amounts of thermal alteration, as indicated by the petrologic type from 3 (no heating) to 6 (most heated). Petrologic types in the range 3–3.9 are unequilibrated (UOCs) and the equilibrated ordinary chondrites (EOCs) of type 4 through 6 have been sufficiently heated with associated mineralogical changes (McSween Jr. & Labotka, 1992). Internal heat within ordinary chondrite parent bodies—produced via the decay of the ^{26}Al radioisotope in the early solar system—created the successive petrologic types that record increasing temperature with increasing burial depth, as the heat buildup created greater temperatures, leaving the surface relatively unaltered (Ghosh & McSween Jr., 1998; McSween Jr. & Labotka, 1992). This scenario has been dubbed the "onion shell" model due to the supposed layers of differing petrologic types within an ordinary chondrite parent body (Miyamoto et al., 1981). The UOCs are the least thermally altered and type 6 have been heated to just short of the metal-sulfide (Fe-FeS) eutectic melting temperature (988°C; Fei et al., 1997; Huss et al., 2006).

In this work, we establish a parameter called the Space Weathering Index (*SWI*), which quantifies the degree of alteration due to space weathering. Akin to the approach of Moroz et al. (1996), we measure the differences between meteorites and irradiated samples using two band parameters diagnostic of space weathering: spectral slope and band depth. To calculate band parameters, we develop a spectral analysis routine that uses a parametric smoothing algorithm to mitigate subjective choices in their calculation. The meteorite spectra are taken from samples having different compositions and petrologic types and sieved into various grain size ranges, allowing us to investigate their effects on spectral band parameters. This large, diverse data set is possible from combining spectra made available from previous studies, for which we perform a meta-analysis of these works.

METHODS

Our investigation targets ordinary chondrites, as their high abundance makes them the most well-characterized meteorite type, and they correspond to S-type asteroids—the most populous asteroid spectral group. The reflectance spectra of material of S-type/ordinary chondrite compositions exhibit characteristic absorption bands positioned near 1 μm (*BI*) and 2 μm (*BII*) due to the presence of olivine and pyroxene (Burns, 1993). From such spectra, we compute spectral parameters that are mostly affected by space weathering (spectral slope and band depth), as well as those that are compositional dependent. It is already well known that *BI* & *BII* positions and band area ratio, or *BAR* (defined as the area of *BII*, BI_A, divided by the *BI* area, BII_A) can be used as diagnostic indicators (e.g., Cloutis et al., 1986). The *BAR* is a well-known diagnostic in approximating the relative abundance of olivine and pyroxene found in ordinary chondrites. In the pioneering work of Gaffey, Bell, et al. (1993), *BAR* and the position of the reflectance minimum of *BI* were used to define asteroid subtypes associated with distinct mineralogic compositions: the so-called ordinary chondrite "boot" shape in this band parameter space encapsulates the H, L, and LL chemical groups. Recent work by McClure and Lindsay (2022) shows that there is a need to independently define the boundaries of this space when different band parameter analyses are implemented, which we do here. Additionally, we investigate other band parameters that can potentially enhance the classification of asteroid spectra into ordinary chondrite chemical types.

Our methods in this work are therefore the following:

- Evaluation of diagnostic band parameters of meteorites that represent unweathered surfaces, or spectrally "fresh" spectra, and for experimentally irradiated meteorite samples that represent space weathered surfaces.
- Development of a multiparameter classification model for classifying ordinary chondrite-like asteroid spectra into H, L, LL, and unequilibrated groups of ordinary chondrites.
- Characterization of changes in spectral slope and band depth using laboratory-irradiated meteorites to quantify a space weathering trend. This will inform the *SWI* parameter formulations.

Data Sources

The NASA Reflectance Experiment Laboratory (RELAB; Pieters & Hiroi, 2004) contains Vis-NIR (~0.32–2.55 μm) reflectance spectra of meteorites. Because the facility makes its services available to others, several hundred meteorite and mineral samples have been sent by investigators for analysis and are subsequently posted in an online database.[1] In this work, we make use of the RELAB database which contains irradiated and unaltered (fresh) ordinary chondrite meteorite spectra (Tables 1 and 2, respectively).

Band Parameter Calculation

Band parameters and their uncertainties are calculated using the Spectral Analysis for Asteroid Reflectance Investigation (SAARI) routine. In the current version of SAARI, *BI* and *BII* are characterized by the wavelength of

TABLE 1. Band parameters of ordinary chondrites.

Meteorite	Type	Fall/ weathering grade	RELAB ID	Grain size	BI_C (μm)	BAR	BII_M (μm)	BI_S (μm^{-1})	BI_D (%)	BI_b (μm)	BI_r (μm)	BII_b (μm)	BI_W (μm)	BII_W (μm)
WSG 95300,64	H3.3	AB	MT-PFV-134-A	<45 μm	0.925	0.268	2.003	0.072	7.4	0.733	1.570	1.614	0.316	0.371
Magombedze	H3.5	Y	TB-TJM-108	<150 μm	0.925	0.804	1.932	−0.001	28.8	0.720	1.478	1.477	0.265	0.479
ALH A77299,91	H3.7	A	MT-PFV-157-A	<45 μm	0.922	0.567	1.955	0.049	9.4	0.742	1.480	1.540	0.273	0.427
Dhajala	H3.8	Y	OC-TXH-020-C	<125 μm	0.928	0.748	1.981	0.126	19.6	0.730	1.483	1.530	0.286	0.506
Dhajala	H3.8	Y	TB-TJM-091	<150 μm	0.926	0.765	1.981	0.083	13.9	0.739	1.478	1.526	0.271	0.532
Dhajala	H3.8	Y	OC-TXH-020-B	125–500 μm	0.921	0.883	1.971	−0.025	19.1	0.727	1.490	1.502	0.295	0.529
Dhajala	H3.8	Y	OC-TXH-020-A	Chip	0.924	0.771	1.975	−0.021	15.8	0.721	1.482	1.518	0.290	0.503
MET 01182,7	H3.8	AB	MT-PFV-159-A	<45 μm	0.930	0.359	1.950	0.040	9.9	0.735	1.510	1.553	0.270	0.351
Suwahib (Buwah)	H3.8	Y	TB-TJM-124	<150 μm	0.920	0.782	1.926	0.050	12.5	0.754	1.422	1.451	0.214	0.532
Avanhandava	H4	Y	TB-TJM-066	<150 μm	0.922	0.811	1.947	0.027	14.6	0.742	1.496	1.508	0.237	0.477
Chela	H4	Y	TB-TJM-071	<150 μm	0.913	0.920	1.962	0.128	25.6	0.729	1.440	1.513	0.225	0.496
Farmville	H4	Y	TB-TJM-128	<150 μm	0.920	0.705	1.913	0.013	16.8	0.704	1.457	1.494	0.253	0.480
Forest Vale	H4	Y	TB-TJM-093	<75 μm	0.930	0.556	1.928	0.043	13.5	0.729	1.535	1.542	0.239	0.444
Kabo	H4	Y	TB-TJM-136	<150 μm	0.925	0.825	1.967	0.018	15.7	0.720	1.479	1.475	0.244	0.508
Marilia	H4	Y	TB-TJM-078	<150 μm	0.920	0.770	1.951	0.034	17.9	0.730	1.455	1.503	0.231	0.476
Monroe	H4	Y	OC-TXH-005-C	<125 μm	0.923	0.665	1.954	0.030	17.4	0.720	1.485	1.520	0.282	0.469
Monroe	H4	Y	OC-TXH-005-B	125–500 μm	0.927	0.961	1.961	−0.112	16.1	0.735	1.490	1.500	0.306	0.512
Ochansk	H4	Y	OC-TXH-008-C	<125 μm	0.922	0.733	1.946	−0.032	20.1	0.725	1.492	1.509	0.280	0.481
Ochansk	H4	Y	OC-TXH-008-B	125–500 μm	0.929	0.871	1.950	−0.139	23.9	0.719	1.492	1.494	0.292	0.506
Ochansk	H4	Y	OC-TXH-008-A	Chip	0.930	0.917	1.964	−0.094	18.6	0.725	1.480	1.502	0.299	0.510
Sao Jose do Rio Preto	H4	Y	TB-TJM-082	<150 μm	0.920	0.959	1.925	0.021	17.9	0.739	1.478	1.500	0.238	0.528
Allegan	H5	Y	TB-TJM-125	<150 μm	0.925	0.777	1.914	0.038	23.2	0.720	1.445	1.475	0.238	0.459
Ehole	H5	Y	OC-TXH-006-C	<125 μm	0.930	0.653	1.914	−0.009	36.1	0.702	1.483	1.485	0.294	0.462
Ehole	H5	Y	TB-TJM-074	<150 μm	0.923	0.927	1.941	0.006	27.4	0.720	1.519	1.500	0.255	0.450
Ehole	H5	Y	OC-TXH-006-B	125–500 μm	0.937	0.608	1.925	−0.067	46.8	0.702	1.503	1.497	0.346	0.490
Ehole	H5	Y	OC-TXH-006-A	Chip	0.927	0.724	1.907	−0.116	34.7	0.701	1.485	1.462	0.313	0.508
Itapicuru-Mirim	H5	Y	TB-TJM-097	<150 μm	0.923	0.775	1.936	0.011	21.2	0.732	1.430	1.490	0.249	0.466
Lost City	H5	Y	TB-TJM-129	<150 μm	0.924	0.788	1.928	−0.001	17.6	0.729	1.467	1.497	0.243	0.475
Olmedilla de Alarcon	H5	Y	OC-TXH-019-C	<125 μm	0.932	0.645	1.960	0.017	20.2	0.725	1.496	1.525	0.297	0.472
Olmedilla de Alarcon	H5	Y	OC-TXH-019-B	125–500 μm	0.932	0.772	1.953	−0.179	24.2	0.715	1.500	1.498	0.309	0.505
Olmedilla de Alarcon	H5	Y	OC-TXH-019-A	Chip	0.923	0.739	1.944	−0.181	21.8	0.705	1.504	1.481	0.287	0.490
Pribram	H5	Y	TB-TJM-143	<150 μm	0.925	0.751	1.915	0.054	19.8	0.726	1.463	1.478	0.253	0.474
Pulsora	H5	Y	TB-TJM-120	<150 μm	0.926	0.742	1.938	−0.004	15.7	0.729	1.466	1.497	0.230	0.455
Schenectady	H5	Y	TB-TJM-083	<150 μm	0.920	0.700	1.906	0.102	26.7	0.739	1.500	1.516	0.235	0.420
Sitathali	H5	Y	TB-TJM-123	<150 μm	0.927	0.736	1.926	−0.006	18.6	0.726	1.480	1.490	0.237	0.458
Uberaba	H5	Y	TB-TJM-085	<150 μm	0.933	0.794	1.944	0.036	19.1	0.738	1.460	1.497	0.244	0.481
Andura	H6	Y	TB-TJM-088	<75 μm	0.915	0.799	1.932	0.088	16.9	0.707	1.439	1.494	0.216	0.470
Butsura	H6	Y	TB-TJM-069	<150 μm	0.920	0.754	1.943	−0.014	14.7	0.737	1.470	1.497	0.229	0.428

TABLE 1. *Continued.* Band parameters of ordinary chondrites.

Meteorite	Type	Fall/ weathering grade	RELAB ID	Grain size	BI_C (μm)	BAR	BII_M (μm)	BI_S (μm^{-1})	BI_D (%)	BI_b (μm)	BI_r (μm)	BII_b (μm)	BI_W (μm)	BII_W (μm)
Canon City	H6	Y	TB-TJM-131	<150 μm	0.934	0.693	1.937	0.031	44.2	0.712	1.490	1.497	0.305	0.494
Chiang Khan	H6	Y	TB-TJM-132	<150 μm	0.928	0.813	1.936	0.007	28.8	0.722	1.478	1.492	0.266	0.479
Guarena	H6	Y	TB-TJM-094	<150 μm	0.920	0.696	1.922	−0.009	35.0	0.710	1.468	1.481	0.282	0.432
Ipiranga	H6	Y	TB-TJM-135	<150 μm	0.925	0.785	1.928	0.029	19.8	0.733	1.466	1.493	0.236	0.465
Nulles	H6	Y	OC-TXH-018-C	<125 μm	0.935	0.560	1.925	0.001	30.8	0.704	1.500	1.515	0.312	0.454
Nulles	H6	Y	OC-TXH-018-B	125–500 μm	0.932	0.733	1.929	−0.161	35.7	0.708	1.495	1.486	0.299	0.492
Nulles	H6	Y	OC-TXH-018-A	Chip	0.938	0.611	1.935	−0.180	30.2	0.705	1.512	1.500	0.320	0.475
QUE 97008,55	L3.05	A	MT-PFV-184-A	<45 μm	0.955	0.264	1.956	0.130	6.8	0.770	1.504	1.585	0.260	0.321
GRO 95544,36	L3.2	AB	MT-PFV-133-A	<45 μm	0.925	0.443	1.961	0.074	8.0	0.735	1.539	1.566	0.264	0.377
GRO 95536,18	L3.3	AB	MT-PFV-140-A	<45 μm	0.935	0.378	1.975	0.057	10.6	0.740	1.505	1.579	0.291	0.390
EET 90628,11	L3.4	AB	MT-PFV-180-A	<45 μm	0.952	0.258	1.961	0.146	6.0	0.762	1.515	1.595	0.291	0.314
Hallingeberg	L3.4	Y	TB-TJM-076	<150 μm	0.956	0.450	1.979	0.068	8.4	0.746	1.560	1.590	0.311	0.460
LEW 85339,10	L3.4	AB	MT-PFV-181-A	<45 μm	0.933	0.401	1.988	0.098	13.2	0.725	1.509	1.565	0.309	0.432
LEW 86505,9	L3.4	A	MT-PFV-142-A	<45 μm	0.925	0.364	1.978	0.071	10.7	0.731	1.532	1.570	0.306	0.429
PRE 95401,13	L3.4	AB	MT-PFV-145-A	<45 μm	0.934	0.423	1.974	0.066	8.8	0.741	1.510	1.560	0.284	0.439
GRO 95504,20	L3.5	AB	MT-PFV-148-A	<45 μm	0.930	0.340	1.962	0.075	7.8	0.731	1.485	1.584	0.274	0.345
GRO 95542,9	L3.5	AB	MT-PFV-149-A	<45 μm	0.927	0.373	1.977	0.067	8.9	0.735	1.525	1.565	0.259	0.343
GRO 95550,6	L3.5	AB	MT-PFV-150-A	<45 μm	0.932	0.398	1.969	0.049	10.7	0.727	1.515	1.560	0.263	0.396
LEW 87284,16	L3.5	A	MT-PFV-182-A	<45 μm	0.927	0.350	1.955	0.034	10.6	0.716	1.503	1.549	0.271	0.414
ALH 85070,8	L3.6	AB	MT-PFV-178-A	<45 μm	0.932	0.473	1.983	0.078	15.4	0.734	1.519	1.560	0.305	0.455
Khohar	L3.6	Y	TB-TJM-138	<150 μm	0.933	0.378	1.964	0.051	11.3	0.720	1.554	1.550	0.291	0.430
MET 00489,12	L3.6	AB	MT-PFV-151-A	<45 μm	0.944	0.347	1.982	0.102	11.9	0.731	1.532	1.590	0.343	0.384
ALH 85155,7	L3.7	AB	MT-PFV-155-A	<45 μm	0.935	0.422	1.986	0.046	11.5	0.732	1.527	1.570	0.311	0.434
Mezö-Madaras	L3.7	Y	TB-TJM-079	<75 μm	0.910	0.580	1.990	0.066	7.4	0.735	1.540	1.575	0.282	0.477
Mezö-Madaras	L3.7	Y	OC-TXH-004-C	<125 μm	0.934	0.443	1.956	0.040	15.0	0.708	1.520	1.543	0.304	0.450
Mezö-Madaras	L3.7	Y	OC-TXH-004-B	125–500 μm	0.939	0.859	1.959	−0.060	15.0	0.732	1.480	1.510	0.267	0.515
Mezö-Madaras	L3.7	Y	OC-TXH-004-A	Chip	0.953	0.763	1.951	−0.152	9.8	0.735	1.509	1.499	0.322	0.514
ALH 84086,27	L3.8	AB	MT-PFV-161-A	<45 μm	0.927	0.558	1.962	0.083	17.2	0.732	1.510	1.540	0.301	0.455
ALH 84120,15	L3.8	AB	MT-PFV-162-A	<45 μm	0.925	0.539	1.961	0.057	17.0	0.726	1.510	1.543	0.309	0.452
ALH 85045,25	L3.8	AB	MT-PFV-163-A	<45 μm	0.930	0.495	1.976	0.087	14.5	0.732	1.506	1.562	0.327	0.446
Atarra	L4	Y	TB-TJM-065	<150 μm	0.920	0.638	1.941	−0.002	26.7	0.739	1.520	1.530	0.301	0.408
Bald Mountain	L4	Y	MR-MJG-044	<150 μm	0.915	0.754	1.980	0.083	12.0	0.729	1.463	1.530	0.239	0.485
Cynthiana	L4	Y	OC-TXH-015-C	<125 μm	0.938	0.512	1.972	0.056	22.4	0.721	1.526	1.550	0.355	0.474
Cynthiana	L4	Y	OC-TXH-015-B	125–500 μm	0.933	0.809	1.959	−0.085	25.4	0.719	1.504	1.512	0.310	0.500
Cynthiana	L4	Y	OC-TXH-015-A	Chip	0.945	0.884	1.973	−0.129	19.9	0.730	1.500	1.508	0.349	0.526
Rio Negro	L4	Y	TB-TJM-081	<150 μm	0.926	0.706	1.939	0.064	23.5	0.731	1.510	1.529	0.262	0.483
Ausson	L5	Y	MT-HYM-084	<150 μm	0.922	0.981	1.926	0.027	24.9	0.727	1.453	1.475	0.223	0.466
Blackwell	L5	Y	MT-HYM-081	<150 μm	0.933	0.486	1.946	0.144	12.4	0.745	1.492	1.565	0.272	0.343
Cilimus	L5	Y	MT-HYM-082	<150 μm	0.928	0.488	1.932	0.040	20.8	0.711	1.524	1.519	0.282	0.421
Elenovka	L5	Y	MS-CMP-013	<75 μm	0.937	0.500	1.935	0.001	32.4	0.693	1.522	1.515	0.321	0.457

TABLE 1. *Continued.* Band parameters of ordinary chondrites.

Meteorite	Type	Fall/ weathering grade	RELAB ID	Grain size	BI_C (μm)	BAR	BII_M (μm)	BI_S (μm^{-1})	BI_D (%)	BI_b (μm)	BI_r (μm)	BII_b (μm)	BI_W (μm)	BII_W (μm)
Elenovka	L5	Y	MS-CMP-041-A	<75 μm	0.936	0.536	1.942	0.005	35.7	0.702	1.516	1.520	0.323	0.466
Guibga	L5	Y	TB-TJM-134	<150 μm	0.933	0.586	1.965	0.027	26.0	0.716	1.509	1.520	0.304	0.487
Honolulu	L5	Y	TB-TJM-096	<150 μm	0.944	0.415	1.960	−0.080	43.7	0.672	1.610	1.600	0.328	0.418
Mabwe-Khoywa	L5	Y	TB-TJM-107	<150 μm	0.928	0.659	1.962	0.019	22.7	0.730	1.500	1.503	0.305	0.460
Malakal	L5	Y	TB-TJM-109	<150 μm	0.930	0.569	1.966	0.057	20.7	0.714	1.517	1.521	0.293	0.486
Messina	L5	Y	TB-TJM-099	<75 μm	0.930	0.533	1.964	0.018	18.9	0.716	1.500	1.520	0.288	0.492
Mirzapur	L5	Y	TB-TJM-111	<150 μm	0.925	0.661	1.946	0.124	19.2	0.682	1.470	1.504	0.278	0.504
Shelburne	L5	Y	TB-TJM-122	<150 μm	0.933	0.615	1.942	0.016	29.0	0.724	1.501	1.518	0.301	0.470
Aïr	L6	Y	TB-TJM-063	<150 μm	0.931	0.512	1.958	0.023	16.2	0.727	1.493	1.527	0.286	0.483
Apt	L6	Y	TB-TJM-064	<150 μm	0.936	0.464	1.943	0.029	31.5	0.718	1.533	1.530	0.305	0.446
Aumale	L6	Y	TB-TJM-101	<150 μm	0.934	0.554	1.948	0.045	30.2	0.714	1.517	1.528	0.307	0.451
Chantonnay	L6	Y	TB-TJM-070	<150 μm	0.929	0.444	1.960	0.031	12.1	0.735	1.620	1.591	0.277	0.444
Château-Renard	L6	Y	OC-TXH-011-C	<125 μm	0.946	0.394	1.943	0.022	29.6	0.701	1.532	1.543	0.356	0.439
Château-Renard	L6	Y	OC-TXH-011-B	125–500 μm	0.944	0.555	1.941	−0.149	38.1	0.696	1.522	1.505	0.328	0.469
Château-Renard	L6	Y	OC-TXH-011-A	Chip	0.960	0.315	1.954	−0.189	34.0	0.686	1.570	1.555	0.428	0.448
Cranganore	L6	Y	TB-TJM-133	<150 μm	0.938	0.479	1.924	0.021	32.6	0.716	1.509	1.514	0.312	0.444
Denver	L6	Y	TB-TJM-072	<150 μm	0.937	0.546	1.957	0.007	16.5	0.712	1.500	1.530	0.282	0.453
Girgenti	L6	Y	TB-TJM-103	<150 μm	0.937	0.477	1.941	0.033	39.1	0.703	1.529	1.529	0.326	0.450
Harleton	L6	Y	OC-TXH-003-C	<125 μm	0.947	0.384	1.944	0.043	33.2	0.695	1.533	1.540	0.361	0.453
Harleton	L6	Y	OC-TXH-003-B	125–500 μm	0.950	0.528	1.944	−0.120	39.9	0.692	1.528	1.517	0.348	0.477
Harleton	L6	Y	OC-TXH-003-A	Chip	0.965	0.320	1.949	−0.160	36.0	0.685	1.570	1.550	0.403	0.453
Karkh	L6	Y	TB-TJM-137	<150 μm	0.938	0.371	1.960	0.003	14.3	0.720	1.533	1.530	0.287	0.430
Kunashak	L6	Y	TB-TJM-139	<150 μm	0.943	0.480	1.948	0.047	30.3	0.713	1.526	1.527	0.330	0.472
Kuttippuram	L6	Y	TB-TJM-098	<75 μm	0.930	0.507	1.944	0.014	23.3	0.704	1.560	1.534	0.288	0.464
Kyushu	L6	Y	TB-TJM-140	<150 μm	0.940	0.496	1.942	0.102	31.8	0.716	1.506	1.526	0.315	0.464
L'Aigle	L6	Y	TB-TJM-141	<150 μm	0.930	0.757	1.955	−0.013	16.9	0.715	1.490	1.519	0.271	0.487
La Criolla	L6	Y	MH-FPF-050-B	<150 μm	0.960	0.485	1.943	−0.071	47.3	0.700	1.578	1.517	0.369	0.489
Maryville	L6	Y	TB-TJM-110	<150 μm	0.942	0.646	1.944	−0.012	38.8	0.701	1.501	1.503	0.328	0.489
Nejo	L6	Y	TB-TJM-112	<150 μm	0.939	0.515	1.936	0.071	40.5	0.697	1.520	1.523	0.339	0.473
New Concord	L6	Y	TB-TJM-130	<150 μm	0.934	0.547	1.926	0.021	31.7	0.720	1.517	1.510	0.305	0.457
Paranaiba	L6	Y	TB-TJM-142	<75 μm	0.930	0.401	1.935	0.109	12.2	0.696	1.479	1.520	0.298	0.500
Patrimonio	L6	Y	TB-TJM-113	<150 μm	0.933	0.615	1.948	0.023	26.5	0.727	1.514	1.525	0.288	0.440
Tuan Tuc	L6	Y	TB-TJM-084	<150 μm	0.910	0.606	1.953	0.074	13.8	0.714	1.450	1.523	0.282	0.471
Valdinizza	L6	Y	TB-TJM-087	<150 μm	0.924	0.499	1.931	0.087	28.6	0.703	1.526	1.533	0.299	0.442
Vouille	L6	Y	TB-TJM-086	<150 μm	0.923	0.515	1.949	0.055	18.2	0.719	1.450	1.550	0.263	0.462
Wethersfield (1971)	L6	Y	TB-TJM-144	<150 μm	0.937	0.345	1.926	0.013	17.4	0.702	1.542	1.540	0.307	0.413
Wethersfield (1982)	L6	Y	TB-TJM-147	<150 μm	0.940	0.543	1.931	−0.015	43.5	0.700	1.516	1.512	0.339	0.472
ALH A76004,41	LL3.3	A	AMT-PFV-137-A	<45 μm	0.937	0.434	1.961	0.033	10.9	0.734	1.530	1.545	0.281	0.442
GRO 95658,17	LL3.3	AB	MT-PFV-141-A	<45 μm	0.936	0.392	1.977	0.112	9.0	0.742	1.522	1.590	0.267	0.355
Chainpur	LL3.4	Y	MR-MJG-067	<45 μm	0.919	0.559	2.009	0.134	8.4	0.740	1.499	1.542	0.271	0.574

TABLE 1. *Continued.* Band parameters of ordinary chondrites.

Meteorite	Type	Fall/ weathering grade	RELAB ID	Grain size	BI_C (μm)	BAR	BII_M (μm)	BI_S ($μm^{-1}$)	BI_D (%)	BI_b (μm)	BI_r (μm)	BII_b (μm)	BI_W (μm)	BII_W (μm)
ALH A78119,35	LL3.5	A	MT-PFV-147-A	<45 μm	0.930	0.402	1.976	0.064	10.5	0.734	1.515	1.578	0.304	0.403
ALH A77278,111	LL3.7	A	MT-PFV-156-A	<45 μm	0.945	0.426	1.985	0.091	13.6	0.734	1.536	1.580	0.342	0.434
GRO 95596,6	LL3.8	AB	MT-PFV-177-A	<45 μm	0.935	0.444	1.978	0.067	14.4	0.734	1.516	1.564	0.325	0.448
Benares(a)	LL4	Y	MT-HYM-083	<150 μm	1.018	0.463	2.001	0.106	19.9	0.728	1.530	1.567	0.410	0.477
Greenwell Springs	LL4	A	TB-TJM-075	<150 μm	0.950	0.447	1.962	0.068	27.3	0.713	1.537	1.555	0.408	0.459
Hamlet	LL4	Y	OC-TXH-002-C	<125 μm	0.945	0.434	1.981	0.143	17.8	0.727	1.534	1.570	0.354	0.453
Hamlet	LL4	Y	MT-HYM-075	<150 μm	0.935	0.492	1.978	0.088	17.4	0.728	1.524	1.557	0.345	0.465
Hamlet	LL4	Y	OC-TXH-002-B	125–500 μm	0.944	0.546	1.976	0.171	14.0	0.735	1.518	1.560	0.340	0.467
Hamlet	LL4	Y	OC-TXH-002-A	Chip	1.050	0.506	2.026	−0.122	12.6	0.730	1.567	1.578	0.481	0.489
Soko-Banja	LL4	Y	OC-TXH-017-C	<125 μm	0.975	0.404	1.979	0.041	30.9	0.711	1.550	1.565	0.455	0.469
Soko-Banja	LL4	Y	OC-TXH-017-B	125–500 μm	0.968	0.565	1.988	−0.084	37.4	0.713	1.545	1.554	0.453	0.505
Soko-Banja	LL4	Y	OC-TXH-017-A	Chip	1.025	0.373	1.973	−0.138	31.4	0.705	1.570	1.570	0.490	0.457
Witsand Farm	LL4	Y	MT-HYM-076	<150 μm	1.025	0.416	2.003	0.078	15.9	0.733	1.544	1.580	0.402	0.449
Aldsworth	LL5	Y	MT-HYM-077	<150 μm	0.936	0.523	1.968	0.052	16.7	0.730	1.520	1.547	0.339	0.450
Alta'ameem	LL5	Y	OC-TXH-010-C	<125 μm	0.985	0.378	1.971	−0.056	37.6	0.695	1.560	1.560	0.470	0.462
Alta'ameem	LL5	Y	MT-HYM-078	<150 μm	0.948	0.412	1.960	0.016	26.1	0.712	1.540	1.550	0.368	0.448
Alta'ameem	LL5	Y	OC-TXH-010-B	125–500 μm	0.976	0.405	1.980	−0.146	37.4	0.696	1.571	1.564	0.477	0.472
Alta'ameem	LL5	Y	OC-TXH-010-A	Chip	1.021	0.264	1.983	−0.177	35.1	0.680	1.605	1.595	0.503	0.451
Olivenza	LL5	Y	OC-TXH-009-C	<125 μm	0.983	0.399	1.972	−0.016	40.6	0.703	1.558	1.565	0.469	0.465
Olivenza	LL5	Y	MT-HYM-085	<150 μm	1.011	0.367	1.979	0.013	26.5	0.712	1.552	1.568	0.429	0.455
Olivenza	LL5	Y	OC-TXH-009-B	125–500 μm	0.976	0.486	1.981	−0.128	40.3	0.704	1.556	1.555	0.458	0.485
Olivenza	LL5	Y	OC-TXH-009-A	Chip	1.028	0.312	1.988	−0.162	33.2	0.695	1.580	1.585	0.495	0.464
Paragould	LL5	Y	OC-TXH-007-C	<125 μm	0.961	0.394	1.986	0.043	10.9	0.650	1.540	1.565	0.329	0.446
Paragould	LL5	Y	MT-HYM-079	<150 μm	0.955	0.407	1.978	−0.030	17.6	0.720	1.542	1.540	0.354	0.453
Paragould	LL5	Y	OC-TXH-007-B	125–500 μm	0.975	0.430	2.017	−0.012	9.6	0.660	1.528	1.535	0.369	0.519
Paragould	LL5	Y	OC-TXH-007-D	Chip	0.978	0.582	1.983	−0.034	11.0	0.701	1.542	1.545	0.390	0.558
Tuxtuac	LL5	Y	MT-HYM-080	<150 μm	1.038	0.270	1.989	0.068	33.8	0.707	1.578	1.599	0.473	0.440
Appley Bridge	LL6	Y	OC-TXH-012-C	<125 μm	1.009	0.274	1.980	−0.020	40.7	0.685	1.585	1.585	0.479	0.447
Appley Bridge	LL6	Y	OC-TXH-012-B	125–500 μm	1.010	0.259	1.995	−0.178	43.3	0.688	1.603	1.589	0.512	0.460
Appley Bridge	LL6	Y	OC-TXH-012-A	Chip	1.009	0.260	1.990	−0.209	35.6	0.690	1.600	1.580	0.466	0.474
Athens	LL6	Y	OC-TXH-013-C	<125 μm	1.019	0.206	1.957	−0.047	33.0	0.680	1.580	1.579	0.458	0.401
Athens	LL6	Y	OC-TXH-013-B	125–500 μm	0.996	0.239	1.977	−0.166	32.6	0.677	1.617	1.585	0.492	0.433
Athens	LL6	Y	OC-TXH-013-A	Chip	1.022	0.185	1.992	−0.161	29.7	0.676	1.624	1.598	0.504	0.421
Bandong	LL6	Y	TB-TJM-067	<150 μm	0.990	0.250	1.976	0.025	21.2	0.699	1.550	1.570	0.388	0.411
Cherokee Springs	LL6	Y	OC-TXH-001-C	<125 μm	0.970	0.315	1.959	−0.007	45.8	0.688	1.571	1.568	0.475	0.437
Cherokee Springs	LL6	Y	TB-TJM-090	<150 μm	0.953	0.386	1.971	−0.022	19.6	0.710	1.566	1.580	0.340	0.452
Cherokee Springs	LL6	Y	OC-TXH-001-B	125–500 μm	0.969	0.414	1.976	−0.142	51.3	0.693	1.565	1.555	0.468	0.487
Cherokee Springs	LL6	Y	OC-TXH-001-A	Chip	0.954	0.517	1.962	−0.161	45.6	0.695	1.534	1.516	0.334	0.501
Chicora	LL6	Y	OC-TXH-014-C	<125 μm	1.011	0.188	1.970	−0.037	27.2	0.686	1.600	1.593	0.455	0.406

TABLE 1. *Continued.* Band parameters of ordinary chondrites.

Meteorite	Type	Fall/ weathering grade	RELAB ID	Grain size	BI_C (μm)	BAR	BII_M (μm)	BI_S (μm^{-1})	BI_D (%)	BI_b (μm)	BI_r (μm)	BII_b (μm)	BI_W (μm)	BII_W (μm)
Chicora	LL6	Y	OC-TXH-014-B	125–500 μm	0.991	0.236	1.975	−0.181	26.5	0.665	1.620	1.570	0.459	0.438
Chicora	LL6	Y	OC-TXH-014-A	Chip	1.021	0.194	2.020	−0.208	22.2	0.690	1.676	1.580	0.477	0.493
Ensisheim	LL6	Y	TB-TJM-092	<150 μm	0.952	0.251	1.971	−0.039	16.1	0.707	1.570	1.570	0.394	0.434
Karatu	LL6	Y	TB-TJM-077	<75 μm	1.000	0.288	1.990	0.005	20.1	0.702	1.590	1.588	0.396	0.466
Saint-Séverin	LL6	Y	TB-TJM-145	<150 μm	0.972	0.256	1.940	0.065	18.4	0.694	1.570	1.546	0.392	0.426

Abbreviations: ALH, Allan Hills; EET, Elephant Moraine; GRO, Grosvenor Mountains; LEW, Lewis Cliff; MET, Meteorite Hills; PRE, Mount Prestrud; QUE, Queen Alexandra Range; WSG, Mount Wisting.

the band minimum and the midpoint, the band depth at the minimum, the spectral slope of a continuum across the band, and the area enclosed by a linear continuum and reflectance values (Figure 1). The routine is similar to that used by Dunn, McCoy, et al. (2010), Sanchez et al. (2015), Popescu et al. (2012) (Modeling for Asteroids, M4AST), and Lindsay et al. (2015; Spectral Analysis Routine for Asteroids, SARA). These routines disagree over the positions of band edges and band centers because their calculations use different order polynomials to define the linear continuum for each absorption feature. A notable distinction from these works is that SAARI utilizes a nonparametric smoothing function to model the reflectance data, which mitigates subjective choice such as which wavelength window is used for polynomial fitting. Another advantage of this approach is its robustness for ground-based astronomical spectra for which the *SNR* may be less than optimal. In particular, the wavelength regions near 1.4 and 1.85 μm at which telluric absorption features decrease the signal relative to other regions (Lord, 1992).

- Step 1: The reflectance values are smoothed using a locally weighted scatterplot smoothing (LOWESS) algorithm (Cappellari et al., 2013; Cleveland, 1979), which fits a second-order polynomial curve to localized subsets of data (within a moving window of 0.1 μm) via least-squares minimization. The smoothed function implements proximal weights using a triangle function in which more outlying data points are given less weight that is linearly proportional to the distance. The magnitude of the reflectance uncertainty is also incorporated into the weighting scheme for which higher noise elements are given less weight. The smoothed function is assessed at increments of $\Delta\lambda = 0.001$ μm to ensure that the spectrum is sampled at intervals smaller than the typical band parameter uncertainties.
- Step 2: Spectral slopes (BI_S and BII_S) are taken as the slope of the linear continua across each band. The short and long wavelength (blue and red, respectively) edges of both bands are determined in the following ways:
  - *BI*: For the 1-μm band, the blue edge is *initially* identified as the maximum reflectance value in the 0.65–0.85 μm range. The red edge is then identified as the tangent point that maximizes the slope of a linear continuum across *BI*. The *final*, reported, blue edge is then chosen as the point where the modeled linear continuum is tangent to the smoothed reflectance curve.
  - *BII*: The red edge of *BII* is held fixed during the entire procedure at 2.45 μm (the spectral noise

TABLE 2. Band parameters of laser and ion-irradiated ordinary chondrites.

Meteorite (+ irradiation dose)	Type	RELAB ID/Ref.	Grain size	Bus-DeMeo taxonomy	BI_C (μm)	BI_S (% μm^{-1})	BI_D (%)	BII_M (μm)	BAR
Appley Bridge (fresh)	LL6	OC-TXH-012-A	Chip	Q	1.009	−0.208	35.5	1.990	0.259
Appley Bridge (+20 mJ)	LL6	OC-TXH-012-A20	Chip	Q	0.997	0.078	23.4	1.978	0.264
Appley Bridge (+2 × 20 mJ)	LL6	OC-TXH-012-A40	Chip	Q	1.001	0.155	22.6	1.978	0.265
Athens (fresh)	LL6	OC-TXH-013-D	125 μm pellet	Q	1.016	−0.182	20.1	1.982	0.280
Athens (+5 mJ)	LL6	OC-TXH-013-D05	125 μm pellet	Q	0.999	−0.024	21.1	1.956	0.246
Athens (+5 + 10 mJ)	LL6	OC-TXH-013-D15	125 μm pellet	Q	1.017	0.000	17.2	1.972	0.234
Burnwell (fresh)	HH4	OC-TXH-021-A	Chip	Q	0.973	−0.175	14.5	1.964	0.516
Burnwell (+20 mJ)	HH4	OC-TXH-021-A20	Chip	K	0.899	−0.007	7.3	1.889	0.513
Burnwell (+2 × 20 mJ)	HH4	OC-TXH-021-A40	Chip	Sq	0.904	−0.076	8.2	1.955	0.767
Château-Renard (fresh)	L6	OC-TXH-011-A	Chip	Q	0.959	−0.189	33.9	1.953	0.314
Château-Renard (+20 mJ)	L6	OC-TXH-011-A20	Chip	Q	0.974	0.041	27.6	1.964	0.298
Château-Renard (+2 × 20 mJ)	L6	OC-TXH-011-A40	Chip	Q	0.964	0.098	25.5	1.945	0.278
Château-Renard (+3 × 20 mJ)	L6	OC-TXH-011-A60	Chip	Q	0.954	0.139	25.0	1.937	0.295
Château-Renard (+4 × 20 mJ)	L6	OC-TXH-011-A80	Chip	Q	0.979	0.159	22.8	1.955	0.301
Château-Renard (fresh)	L6	OC-TXH-011-D	125 μm pellet	Q	0.949	−0.125	22.1	1.946	0.437
Château-Renard (+5 mJ)	L6	OC-TXH-011-D05	125 μm pellet	Q	0.948	0.000	21.7	1.930	0.421
Château-Renard (+5 + 10 mJ)	L6	OC-TXH-011-D15	125 μm pellet	Sq	0.944	0.146	18.3	1.933	0.409
Château-Renard (+5 + 10 + 20 mJ)	L6	OC-TXH-011-D35	125 μm pellet	Sq	0.938	0.255	16.9	1.936	0.389
Cynthiana (fresh)	L4	OC-TXH-015-D	125 μm pellet	Q	0.939	−0.120	16.7	1.978	0.544
Cynthiana (+5 mJ)	L4	OC-TXH-015-D05	125 μm pellet	Sq	0.934	−0.009	16.2	1.960	0.536
Cynthiana (+5 + 10 mJ)	L4	OC-TXH-015-D15	125 μm pellet	S	0.929	0.142	14.0	1.935	0.491
Ehole (fresh)	H5	OC-TXH-006-A	Chip	Q	0.927	−0.115	34.7	1.906	0.724
Ehole (+20 mJ)	H5	OC-TXH-006-A20	Chip	Q	0.938	0.055	19.3	1.922	0.588
Ehole (+2 × 20 mJ)	H5	OC-TXH-006-A40	Chip	Q	0.932	0.032	24.3	1.907	0.849
Elenovka (fresh)	L5	MS-CMP-041-A	<75 μm	Q	0.937	0.001	32.3	1.934	0.499
Elenovka (+1.2 kW)	L5	MS-CMP-041-B	<75 μm	Q	0.939	0.092	34.7	1.935	0.511
Hamlet (fresh)	LL4	OC-TXH-002-A	Chip	Q	1.050	−0.121	12.6	2.025	0.506
Hamlet (+20 mJ)	LL4	OC-TXH-002-A20	Chip	S	1.036	0.131	17.3	2.006	0.399
Hamlet (+2 × 20 mJ)	LL4	OC-TXH-002-A40	Chip	S	1.035	0.171	16.8	1.994	0.365
Hamlet (+3 × 20 mJ)	LL4	OC-TXH-002-A60	Chip	S	1.040	0.216	16.3	1.995	0.344
Hedjaz (fresh)	L3.7	OC-TXH-016-A	Chip	Q	0.922	−0.126	20.4	1.955	0.923
Hedjaz (+20 mJ)	L3.7	OC-TXH-016-A20	Chip	Sq	0.917	−0.071	16.5	1.908	0.786
Hedjaz (+2 × 20 mJ)	L3.7	OC-TXH-016-A40	Chip	S	0.913	−0.011	12.8	1.960	0.793
Epinal (fresh)	H5	Strazzulla et al. (2005)	Chip	Q	0.932	0.08	29.7	1.911	0.535
Epinal (+1.3 × 10^{15} Ar^{++})	H5	Strazzulla et al. (2005)	Chip	Sq	0.934	0.215	28.1	1.915	0.549
Epinal (+4.3 × 10^{15} Ar^{++})	H5	Strazzulla et al. (2005)	Chip	Sq	0.932	0.369	26.6	1.914	0.552
Epinal (+1.7 × 10^{16} Ar^{++})	H5	Strazzulla et al. (2005)	Chip	Srw	0.932	0.218	28.5	1.915	0.558
Kosice (fresh)	H5	Kanuchova et al. (2015)	Bulk	Q	0.930	−0.099	28.8	1.947	0.787
Kosice (+2.7 × 10^{14} Ar^{+})	H5	Kanuchova et al. (2015)	Bulk	Q	0.939	−0.076	27.5	1.946	0.828
Kosice (+4.0 × 10^{15} Ar^{+})	H5	Kanuchova et al. (2015)	Bulk	Sr	0.941	−0.024	24.6	1.926	0.758
Kosice (+1.0 × 10^{16} Ar^{+})	H5	Kanuchova et al. (2015)	Bulk	Sr	0.938	0.035	23.7	1.942	0.886
Kosice (+5.0 × 10^{16} Ar^{+})	H5	Kanuchova et al. (2015)	Bulk	S	0.926	0.185	16.5	1.966	0.940

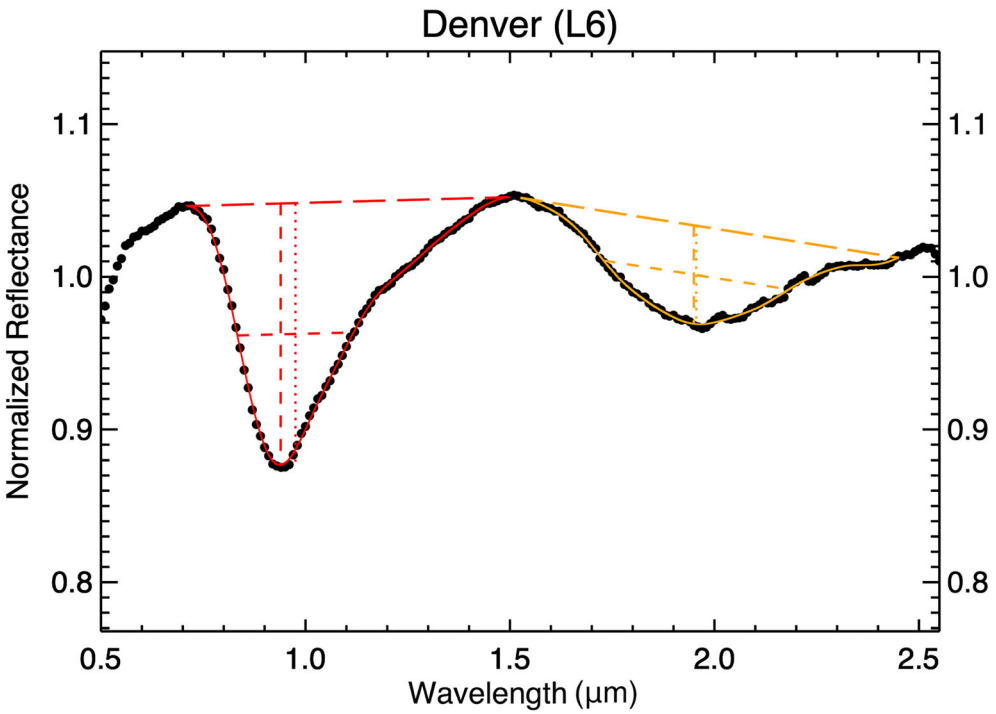

FIGURE 1. Depiction of band parameters for Denver (L6) as calculated with SAARI for *BI* (red) and *BII* (yellow). Long dashed lines are model continua, short dashed lines indicate band widths at half-minimum, dash-dot lines are band minima, and dotted lines are band midpoints. The band minima and midpoints are marked for clarity. (Color figure can be viewed at wileyonlinelibrary.com)

drastically increases for several astronomical spectrographs at $\lambda > 2.45$ μm) and the blue edge of *BII* is identified where the linear continuum lies tangent to the smoothed reflectance function.

- Step 3: The reflectance values across each band are divided by their respective modeled linear continua, and the band centers (BI_C and BII_C) are identified as the wavelength of the minimum of the smoothed, continuum-divided reflectance. It is worth noting here that BII_C is likely not the *true* minimum of *BII* because of the fixed red edge cutoff at 2.45 μm (Lindsay et al., 2015; McClure & Lindsay, 2022), which is short ward of the true edge of the absorption feature that lies beyond 2.55 μm.
- Step 4: Band depths (vertical short dashed lines in Figure 1) for each respective band (BI_D and BII_D) are calculated from the minimum reflectance after dividing by the continuum, R_m, as follows: $B_D = 1 - R_m$.
- Step 5: The full width at half-minimum (referred to hereafter simply as the band width: BI_W and BII_W) of each band is calculated by measuring the width, in microns, at which the continuum-divided reflectance is halfway to the minimum value. This parameter is shown as short dashed lines in Figure 1.
- Step 6: Band midpoints (BI_M, BII_M) are defined by the center wavelength at half-minimum. Band midpoints, shown as dotted lines in Figure 1 do not necessarily, and often do not, correspond to band centers.
- Step 7: Band areas (BI_A and BII_A) are computed by integrating the region enclosed by the continuum-divided reflectance values and the linear continuum. The band area ratio, *BAR*, is computed via $BAR = BII_A/BI_A$.

RESULTS

All of the available RELAB meteorite spectra were acquired with a very high *SNR* (>100) and sample-to-sample variations are dominant over any band parameter uncertainties. Therefore, we report meteorite band parameters without individual uncertainties. Band parameters of fresh (unirradiated) and irradiated meteorite spectra are given in Tables 1 and 2, respectively. The terrestrial weathering grade (A, AB, B, C in the ANSMET system; Harvey, 2003) of each sample is given unless it was an observed fall (marked as "Y"). The RELAB ID, which contains information about the sample for each experiment/PI is given for each sample.

In total, we analyzed 195 ordinary chondrite spectra from RELAB (162 fresh and 33 irradiated), with samples from all chemical groups (H, L, and LL), petrologic types (3 through 6), and various particle size ranges. Meteorite

spectra were collected for samples that had been sieved into various, distinct size bins: <45 μm, <75 μm, <125 μm, <150 μm, and 125–500 μm. In addition, some samples are not ground into powders but left as centimeter-scale chips. All chemical groups and petrologic types are represented. We noted the petrologic type of all samples as listed in the Meteoritical Bulletin Database[2] on January 30, 2023. Finally, we are using only the meteorites reported as falls, or that have a weathering grade of "A" or "AB" because of the considerable effect that terrestrial weathering products have on these spectral parameters (e.g., Lucas et al., 2019).

Next, we focus on two sets of band parameters: those that are characteristic of space weathering (BI_S and BI_D; Gaffey, 2010) and those that are indicative of mineralogy (band midpoints, band minima, and *BAR*; Gaffey et al., 2002). From our analyses, we seek to identify dependencies on the grain size and petrologic type of meteorites. The findings are used to inform a band parameter-based spectral classification model, followed by the development of the *SWI*.

Space Weathering Band Parameters

We look for statistically significant dependencies of the band depth and slope on grain size and petrologic type using a two-way analysis of variance (ANOVA; Fisher,1919) test in the R package "car". A two-way ANOVA calculates how much of the variance in a quantitative dependent variable (in our case, BI_S and BI_D) can be explained by two categorical independent variables (grain size and petrologic type). The null hypothesis is that the means are no different and, alternatively, that the mean are different. We also test for possible interaction between the independent variables in the ANOVA, in which changes in one variable are partly dependent on the other.

For this part of our analysis, we use only the spectra from powdered <75 μm, <125 μm, 125–500 μm grain size bins and spectra from meteorite chips. In doing so, we (1) reduce the risk associated with different sample preparation from various experiments and (2) optimize the variation in band parameters from grain size differences by using mutually exclusive (the <125 μm and 125–500 μm bins) or drastically different sizes (<75 μm powder and chips). An example of the former is that metal grains were removed by Dunn, McCoy, et al. (2010), which led to a decrease in the band depth of their <150 μm powdered samples (figure 3.5 in MacLennan, 2019). We plot the distributions of band slopes and depths as a function of these size bins and petrologic type in Figure 2. Lines connect data points that represent the same meteorite in which spectra were available for different grain sizes (or chip). See Table 1 for details about these samples.

A summary of the *F*-statistics (variation between sample means and the intragroup variation) and *p*-values in parentheses is given in Table 3. Higher values of the *F*-statistic indicate that the independent variable accounts for more of the variation in the sample and is thus a significant factor. Lower *p*-values indicate a higher statistical significance (1-*p* gives the probability that the alternative hypothesis of different means is supported). We also considered chemical groups in this analysis but found no correlation between these two space weathering parameters.

The most apparent trend is that between the grain size and the spectral slope, which is also indicated by the large *F*-statistic (Table 3). The chips preferentially show negative (bluer) spectral slopes and slopes in the smallest size bin are the largest (reddest). This trend is present for each petrologic type, although type 5 samples show a weaker trend. While there is a decrease in BI_S with higher petrologic type (for the same grain size/chip), this trend is not always apparent across all petrologic types and grain sizes. For example, when looking at the smallest grain size bin, one does not observe a clear difference in BI_S with petrologic type. However, the trend between BI_S and petrologic type becomes stronger for larger grain sizes. This interaction between grain size and petrologic type is indicated in Table 3 and is consistent with increased olivine abundance (Gaffey, Bell, et al., 1993) and Fe-Ni metal content (Gaffey, Burbine, & Binzel, 1993) for higher petrologic types. However, we do not see any clear BI_S changes with chemical group, where olivine and metal abundances are more varied than with petrologic type (McSween Jr. & Labotka, 1992).

Similar to the spectral slope results, we find that BI_D is dependent on both the grain size and the petrologic type. This band depth dependency is stronger for petrologic type (higher *F*-statistic) than for grain size: higher petrologic types show greater band depths, on average. Our results are very consistent with Eschrig et al. (2022) for both dependencies. For each petrologic type except for type 5, an increase in band depth is seen for the powdered samples, and a decrease for spectra of the chips. This trend is the weakest for the UOCs (types 3–3.9), which exhibit the weakest absorption band features compared to all other petrologic types. The petrologic type versus BI_D trend for <75 μm samples is not clear, given that only one spectrum for types 3–3.9 and type 4 exists, and the BI_D values for type 6 OCs are smaller. We also analyze the BI_D values for the UOCs with <45 μm grain sizes (Vernazza et al., 2014, RELAB ID beginnings with "MT-PFV" in Table 1) in Figure 3 to confirm that this trend extends to lower grain sizes and petrologic types. There is a clear increasing trend in BI_D for petrologic types larger than 3.5 (Figure 3), which most likely corresponds to chemical changes caused by metamorphic heating above 400°C (Vernazza et al., 2014).

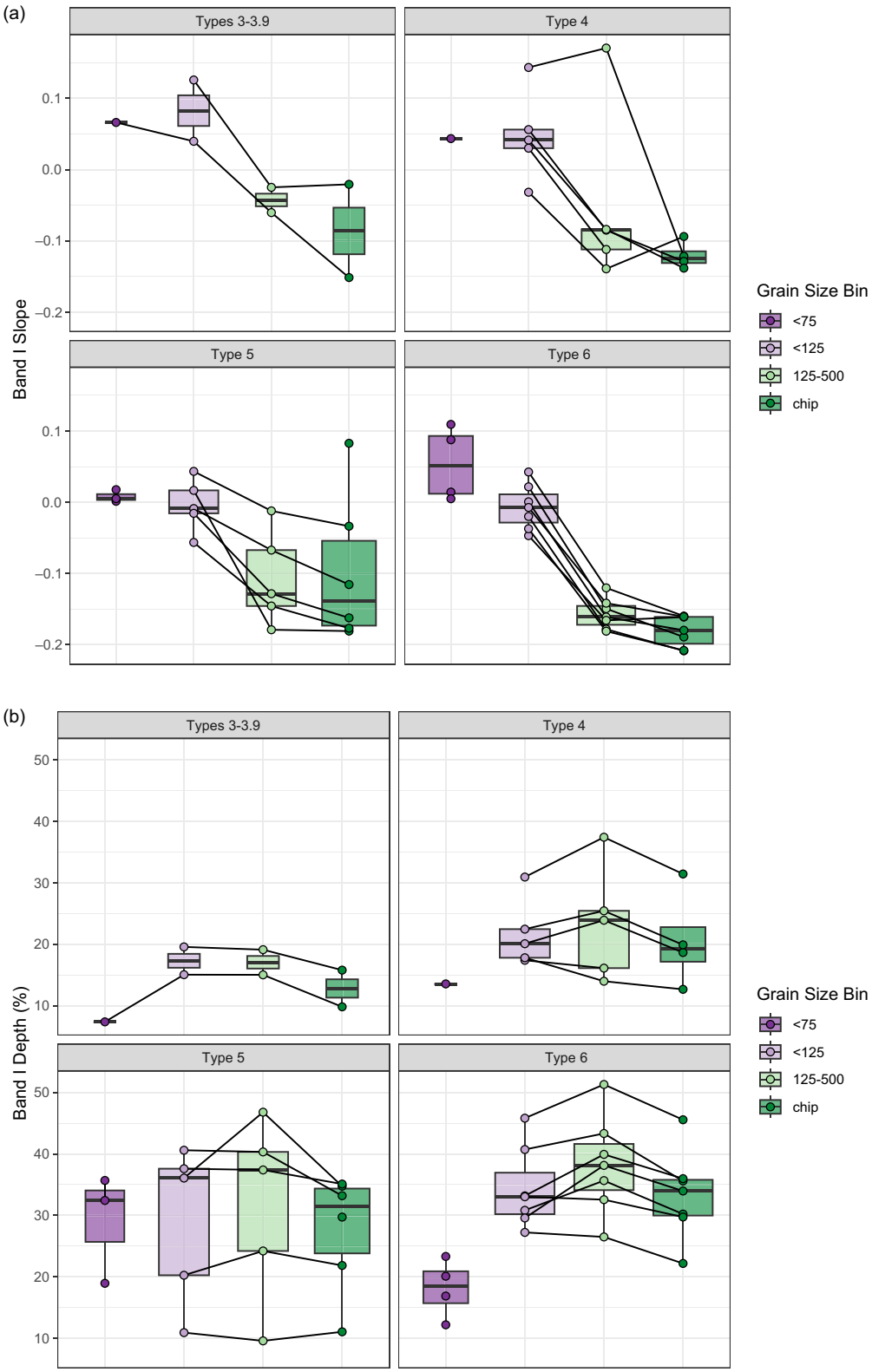

FIGURE 2. Band I slopes (a) and depths (b) of ordinary chondrites as a function of the grain size of the sample, separated by petrologic types. Lines connect the same meteorite that has been sieved into different size bins. Box-whisker representations show the quartile ranges and median for the samples in each grain size bin. (Color figure can be viewed at wileyonlinelibrary.com)

TABLE 3. ANOVA results, *F*-statistic (*p*-value). (Color table can be viewed at wileyonlinelibrary.com)

	Pet. type	Grain size	Interaction
BI_S	8.376 (<0.001)	35.135 (<0.001)	2.551 (0.006)
BI_D	14.223 (<0.001)	5.115 (<0.001)	1.024 (0.429)

Note: Shaded cells indicate a statistically significant result.

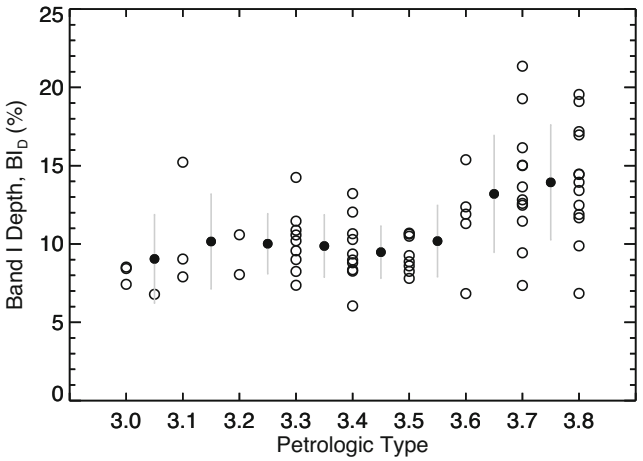

FIGURE 3. BI_D as a function of petrologic type for unequilibrated ordinary chondrites (UOCs). Open circles are measurements for individual spectra and filled circles are averages of adjacent bins with sample standard deviation shown by the vertical bars.

Compositional Band Parameters

We now extend our analysis to the many band parameters that are diagnostic of mineralogy, notably the band positions and band area ratio, *BAR*. Similar to our approach in the last subsection, we wish to examine the potential effects of grain size and petrologic type on this set of parameters using ANOVA testing. These independent variables are unbalanced, meaning they do not have equal sample sizes. Thus, for each of the ANOVA tests, different permutations of the independent variable were considered, in order to find the sequence that prioritizes the most statistically significant effect. For this analysis, we reintroduce the spectra from the Dunn, McCoy, et al. (2010) <150 μm metal-free powders, noting that the band positions and *BARs* don't deviate from the other samples from the same groups (MacLennan, 2019). Therefore, including them here will not skew the results as they did in the analysis of the previous subsection.

In addition to the traditionally used BI_C and *BAR* to discern between OC chemical groups, we consider band parameters not often used for compositional studies—the positions of the band edges: the red and blue edges of *BI* (BI_b and BI_r) and blue edge of *BII* (BII_b). We also use the *BII midpoint* (BII_M) as opposed to the *center* because telluric water vapor significantly increases the noise where

TABLE 4. ANOVA results, *F*-statistic (*p*-value). (Color table can be viewed at wileyonlinelibrary.com)

	Chem. group	Pet. type	Grain size
BI_C	151.3 (<0.001)	1.2 (0.324)	6.2 (<0.001)
BAR	160.6 (<0.001)	17.4 (<0.001)	5.0 (<0.001)
BII_M	87.0 (<0.001)	13.3 (<0.001)	1.5 (0.195)
BI_r	97.1 (<0.001)	4.4 (0.005)	*3.8 (0.005)
BI_b	23.8 (<0.001)	28.2 (<0.001)	*11.4 (<0.001)
BII_b	134.2 (<0.001)	2.4 (0.056)	2.0 (0.114)
BI_W	253.5 (<0.001)	*3.9 (0.010)	19.7 (<0.001)
BII_W	*5.7 (0.004)	9.9 (<0.001)	6.5 (<0.001)

Note: All shaded cells indicate a statistically significant result.
*Result changes to nonsignificant when <150 μm bin is removed.

BII band centers (i.e., reflectance minima) are often found (1.8–1.95 μm). By selecting the band midpoint, which is calculated using the sides of the band (i.e., the center at half-minimum), this uncertainty is mitigated. In addition, some investigations have noted that the spectra of UOCs show spectral signatures of two distinct pyroxenes (orthopyroxene and clinopyroxene) in *BII*, whereas EOCs do not (Gietzen et al., 2012; Sears et al., 2021). Being dependent on the sides of the band, rather than the minimum value, the midpoint is sensitive to this spectral variation and is therefore sensitive to the pyroxene compositions.

Table 4 gives a summary of the *F*-statistics and *p*-values in parentheses for the ANOVA tests using three independent variables (chemical group, petrologic type, and grain size) for each band parameter. Figures 4 and 5 also show the relationship between each parameter with grain size and petrologic type, respectively. We find that grain size has a small, but statistically significant, effect on both the BI_C and *BAR*. Such a correlation has been noted for HED meteorites (Bowen et al., 2023; Duffard et al., 2005). These two band parameters are the typical default analysis tool to discern between different mineralogical compositions of S-complex asteroids. The band widths are also seen to vary with grain size, which agrees with Gaffey et al.'s (2015) analysis of terrestrial olivine.

In addition to the chemical group, we find that most of the band parameters considered are influenced by the petrologic type; notably the *BAR*, BI_b, BII_M, and BII_W. Our results are not surprising for *BAR* and BII_M, as these parameters are influenced by the olivine/pyroxene abundance ratios (Gaffey, Bell, et al., 1993) which have been shown to increase with higher thermal alteration within each chemical group (Dunn, McSween Jr., et al., 2010). The modal increase in olivine relative to orthopyroxene for higher petrologic types is due to progressive oxidation with increasing thermal metamorphism (Rubin, 1990). Although, it is seen that the variation in relative mineral abundances *between* groups is larger than the variation *within* each of them.

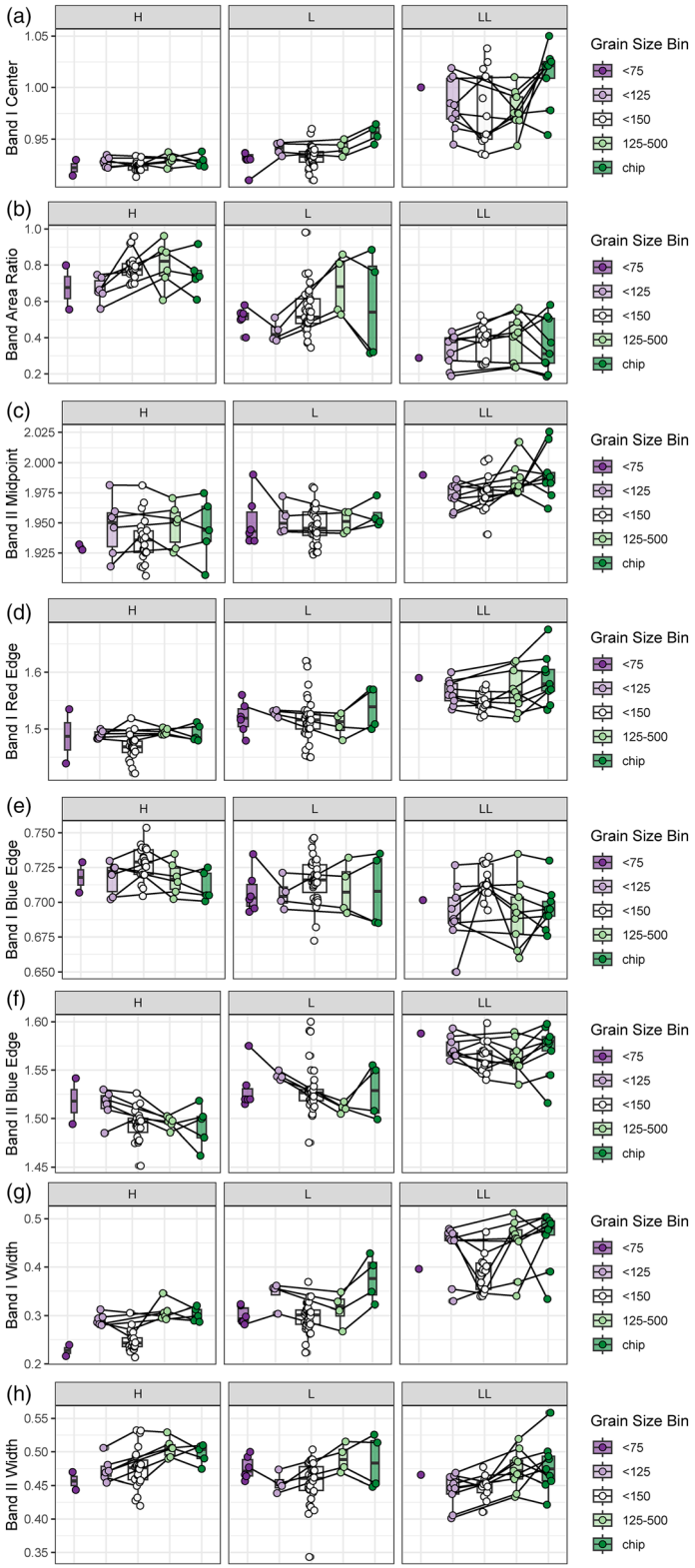

FIGURE 4. Band parameters for different chemical groups, separated by grain size: (a) band I minimum, (b) band area ratio, (c) band II center, (d) band I red edge, (e) band II blue edge, (f) band I blue edge, (g) band I width, and (h) band II width. Box-whisker representations show the quartile ranges and median for the samples in each grain size bin. (Color figure can be viewed at wileyonlinelibrary.com)

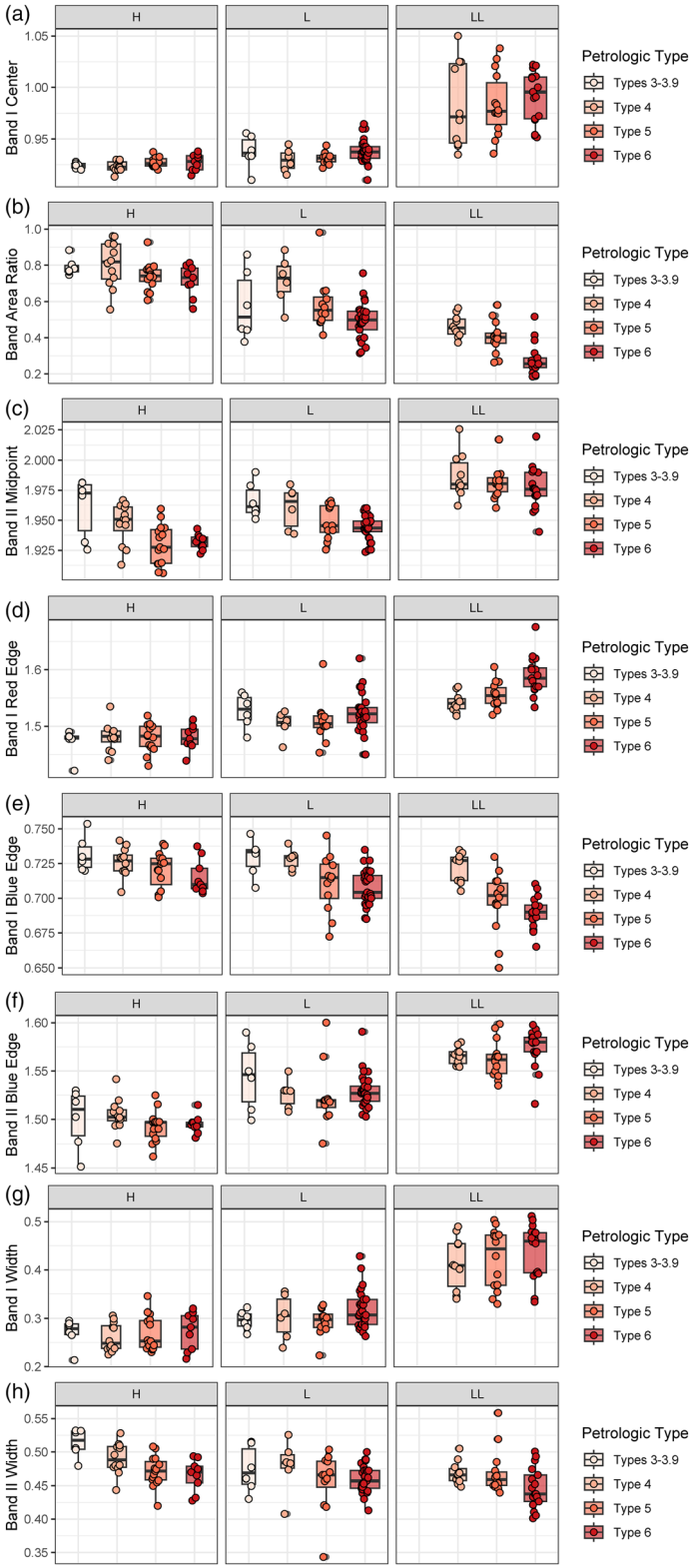

FIGURE 5. As in Figure 4 but organized by petrologic type. Box-whisker representations show the quartile ranges and median for the samples in each petrologic type. (Color figure can be viewed at wileyonlinelibrary.com)

Interestingly, the BI_b position and BII_W are mostly influenced by petrologic type over the chemical group.

The ANOVA test is advantageous for identifying differences among categorical groups but cannot necessarily identify trends for ordinal variables. We inspect the group variations in BAR, BII_M, BI_r, and BII_b and find many of these variables show some correlation with the petrologic type, but the strength depends on the chemical group. These findings, while seemingly complex at first glance, can be used in a supervised spectral classification model that predicts chemical group *and* petrologic type from band parameters, which we perform in Petrologic Type Classification Section. First, we demonstrate such an approach for a simpler case of chemical groups in the next subsection.

Chemical Group Classification

It has been shown that band parameter model choices can have noticeable effects on band parameter estimations (e.g., McClure & Lindsay, 2022). We define a customized set of criteria from SAARI band parameters shown in Figure 5. Comparing our results with that of Gaffey, Bell, et al. (1993), the differences in band parameter calculation methods correspond to a change in the location of the ordinary chondrite boot (Figure 6a). In addition to the traditional BI_C and BAR parameters, we also incorporate the BII midpoint (Figure 6b), as we have shown that it is not affected by the grain size. Additionally, this parameter is useful in distinguishing H chondrites from the acapulcoite and lodranite clans (Lucas et al., 2019), as opposed to using only BI_C and BAR. The band parameter data sets shown in Figure 6 are marked by UOC classification or, if an EOC, into three chemical groups: H, L, and LL. One meteorite, Cynthiana, is ambiguously classified as an L/LL, but its band parameters are clearly more similar to those of L chondrites, so we treat it as such in the analysis.

We use a linear discriminant analysis (LDA) to classify spectra into four groupings: H, L, LL, and UOC. This method computes a linear combination of input variables (linear components) that maximizes the distance between known classes in linear discriminant coordinates (Fisher, 1936). As opposed to an unsupervised principal component analysis (PCA), which maximizes the variation across an entire data set, the LDA algorithm is optimized for classification of data sets into a priori groupings (i.e., H, L, LL, and UOC) by maximizing the variance *between* these groupings.

Initially, we treat all samples in the data set according to their chemical group (H, L, or LL). Using the BI_C, BII_M, and BAR as independent band parameters in the LDA, we observe that the prediction accuracy for the L group increases by removing the UOCs. It is interesting to note here that different chemical groups within the UOCs diverge from their EOC counterparts, and they have previously been shown to be spectrally similar to equilibrated L chondrites (Vernazza et al., 2014). In a second iteration, we treat the UOCs as a *distinct* grouping with all chemical groups included (i.e., H3-3.9, L3-3.9, and LL3-3.9 are all treated as one UOC grouping). Because of this modification, as shown below, the

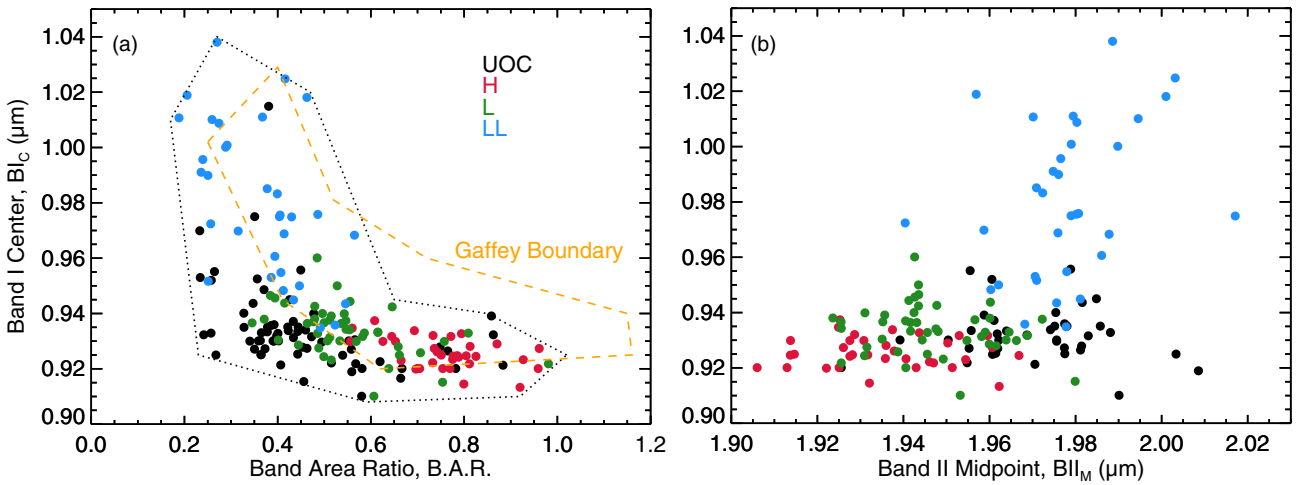

FIGURE 6. Ordinary chondrite BI_C with BAR (a) and BII_M (b) values calculated using the SAARI routine. Colors indicate the chemical group (H, L, or LL) of EOC samples and black symbols represent UOCs from all three chemical groups. The boundary of the Gaffey, Bell, et al. (1993) ordinary chondrite boot is shown as a dashed orange line in panel (a). (Color figure can be viewed at wileyonlinelibrary.com)

prediction accuracy for the L chondrites is comparable to that of the H and LL groupings.

The LDA model calculates three linear discriminant (*LD*) functions, or dimensions, by multiplying the input band parameters by coefficients. We have taken the additional step to normalize the LD functions by subtracting the means of each as follows:

$$LD1 = 29.050\ BI_C + 34.775\ BII_M - 3.219\ BAR - 93.850, \quad (1(a))$$

$$LD2 = -55.554\ BI_C + 38.204\ BII_M - 4.767\ BAR - 19.746, \quad (1(b))$$

$$LD3 = -2.606\ BI_C - 40.228\ BII_M - 5.542\ BAR + 84.222. \quad (1(c))$$

Therefore, in order to classify any set of band parameters, one calculates the linear discriminant values and compares them to the mean values for each grouping in Table 5.

The classification results for our sample are summarized as a confusion matrix in Table 6 with the number of samples for the true (known) and predicted groupings are given in the rows and columns, respectively. The diagonal values represent true positives, and nondiagonal values are false positives. For example, of the 37 total H chondrite spectra, 31 were correctly classified, and of the 41 spectra that are predicted to be an H chondrite, 10 are from other groupings: five UOCs and five L types. The bottom row gives the balanced success rate, which is an average of the true positive rate —the correct prediction rate of a sample in the true grouping—and the true negative rate—the correct rejection rate of a sample not in the true grouping for each grouping.

The linear discriminant plot shown in in Figure 7 shows the true classes of samples as symbol labels and predicted classes as colors. For example, a correctly classified UOC spectrum is represented by a black "U", and a red "U" indicates a misclassification in the H grouping. Because *LD1* and *LD2* together explain over 97% of the intergroup variation, Figure 7a best shows

TABLE 5. Mean values of linear components for each grouping in the LDA model.

	LD1	*LD2*	*LD3*
H	−2.059	−0.928	−0.574
L	−0.612	0.045	0.778
LL	3.128	−1.047	−0.160
U	0.499	1.473	−0.186

TABLE 6. Confusion matrix and balanced success rate statistic of the LDA classification. The cells show the number of samples in the true (rows) and predicted (columns) classes.

		Predicted grouping			
True grouping		H	L	LL	UOC
	H	31	5	0	0
	L	5	34	0	8
	LL	0	4	30	7
	UOC	5	4	0	30
		85.7%	80.6%	95.8%	79.1%
		Balanced success rate			

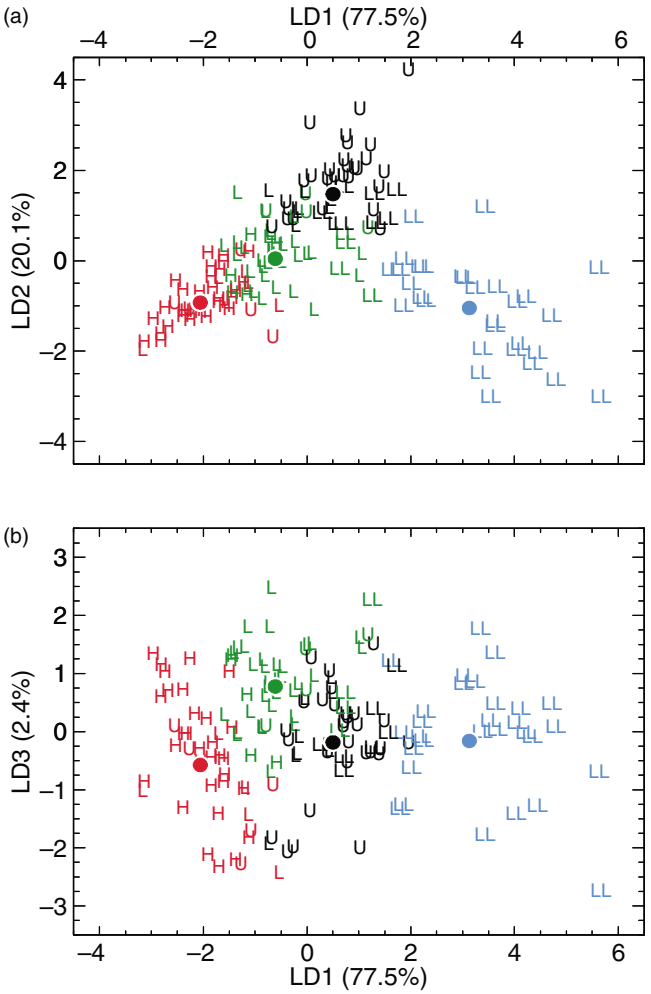

FIGURE 7. Linear discriminant values for ordinary chondrite groups. The values in parentheses are the between-class variance explained by each linear discriminant coordinate. Symbols indicate the predicted classification of each sample, based on the proximity to the group averages shown by the colored star symbols. The red, green, blue, and black colors indicate the true grouping (H, L, LL, or U = unequilibrated, respectively). (Color figure can be viewed at wileyonlinelibrary.com)

the separation of the classes. The L chondrites and UOCs are most difficult to correctly classify as they have band parameters that are situated between all other groups. Although four LL chondrites are misclassified in the L group, and seven being misclassified as UOCs (Table 6), the true positive rate is 100%. This occurrence is most likely due to the clear separation in linear discriminant space from the other groupings (Figure 7a).

We note that false positives (10 of 41 for H, 13 of 47 for L, 0 of 30 for LL, and 16 of 45 for UOC) are mitigated by using meteorites that are observed falls or with minimal signs of weathering (a grade of A or AB). This is because weathered meteorite spectra have band parameters that deviate significantly from others in their grouping. Therefore, we strongly advise future studies to consider the mitigation of terrestrial weathering effects (i.e., Lucas et al., 2019) for meteorite spectral band parameters. Finally, we point out that 9 UOCs were classified as in H, L, or LL chemical groups. However, some of these UOCs are correctly predicted to into their actual chemical group (e.g., a type 3–3.9 H chondrite is classified as an H instead of UOC). Considering this fact, the true positive rates of the H, L, and LL groups are somewhat higher than those presented in Table 6.

Petrologic Type Classification

Motivated by our finding that some band parameters are influenced by the petrologic type, in addition to the chemical group, we employ a LDA model to formulate a classification scheme for discerning both the chemical group and the petrologic type. For this model, we only select the band parameters from EOC samples, noting that doing so removes all samples from the <45 μm grain size fraction. This still provides us with a large set of band parameters from 125 EOC meteorite spectra.

In total, there are nine groupings for which the LDA will consider, making it more challenging to accurately separate them compared to the classification model in the previous subsection. To improve the model accuracy, we include several more band parameters, such as the band edges and widths: BI_C, BI_r, BI_b, BAR, BII_M, BII_b, BI_W, and BII_W. As we have shown in Compositional Band Parameters Section, some of these parameters are highly dependent on chemical group, but some are affected mostly by the petrologic type (BI_b and BII_W). Using eight independent variables to classify into nine groupings avoids the potential risk of model overfitting.

The first four *LD* functions, which encapsulate 98% of the total variation, are formulated using the linear discriminant coefficients given in Table 7. Each coefficient is multiplied by the relevant band parameter, as done in Equations 1(a)–1(c). The bottom half of Table 7 gives the mean values of each *LD* axis for all groups, similar to that in Table 5.

TABLE 7. LDA coefficients and mean values for each grouping.

	LD1	*LD2*	*LD3*	*LD4*
BI_C	−5.013	−1.734	47.493	11.597
BI_r	−7.325	−14.243	−5.434	−17.406
BI_b	2.912	30.331	−17.335	63.908
BAR	−5.048	7.916	3.816	−9.207
BII_M	32.804	16.007	−1.189	−33.660
BII_b	16.945	31.193	−36.579	−7.192
BI_W	11.123	13.133	4.932	5.880
BII_W	2.989	3.996	−23.535	21.157
H4	−2.300	1.317	−0.279	−0.448
H5	−2.685	−0.081	0.718	0.324
H6	−2.480	−0.212	0.802	−0.102
L4	−0.798	1.722	−0.821	−0.407
L5	−0.856	−0.431	−0.328	−0.492
L6	−0.295	−1.010	−0.564	0.349
LL4	2.631	1.957	0.004	0.781
LL5	2.647	0.457	0.295	−0.179
LL6	3.126	−0.849	0.336	−0.351

The confusion matrix for this LDA (Table 8) shows the true and predicted groupings of each of the nine EOC groupings. The most challenging group to predict is the L5, as they have band parameters that lie in the center of the entire data set, which comprises a compositional continuum of varying olivine and pyroxene abundances (see discussion in Discussion Section).

The balanced accuracies across all groups are greater than 70%, which is encouraging. However, truly assessing the accuracy of this LDA is challenging due to the small sample sizes that comprise each grouping (for example, there are only six L4 meteorites in this sample). Future work will incorporate more spectra, consider independent variable interactions, and consider other classification schemes like machine learning to improve upon this classification model.

The Space Weathering Index

We now formulate a parameter called the *SWI* that is intended to encapsulate the extent, or degree, of space weathering for an asteroid spectrum. The *SWI* is based on the separation between the weathered asteroids and fresh meteorites as measured using BI_S and BI_D values. The separation metric is assessed along the approximate direction of spectral changes for irradiated meteorites (Figure 9a). A zero point for the *SWI* coordinate is established using the space weathering parameters of the fresh meteorites analyzed herein, which are shown in Figure 9b. Differences in spectral slope among the grain

TABLE 8. Confusion matrix for the chemical group and petrologic type LDA.

		Predicted grouping								
True grouping		H4	H5	H6	L4	L5	L6	LL4	LL5	LL6
	H4	8	2	0	0	1	1	0	0	0
	H5	2	11	0	0	1	2	0	0	0
	H6	0	5	3	0	0	1	0	0	0
	L4	2	0	0	2	1	0	1	0	0
	L5	0	1	0	0	4	7	0	0	0
	L6	1	0	0	0	1	26	0	0	1
	LL4	0	0	0	0	0	0	8	2	0
	LL5	0	0	0	0	0	2	1	8	2
	LL6	0	0	0	0	0	1	0	1	13
		79.0%	76.6%	97.5%	81.7%	71.6%	79.2%	89.1%	83.7%	88.8%
		Balanced success rate								

size bins make it inherently difficult to determine this zero point. We arbitrarily choose the slopes of the <150 μm grain size bin because all petrologic types are well represented.

A second coordinate called the band depth index (*BDI*) is established and is aligned with the set of meteorite samples. It is named as such because it is highly dependent on the BI_D, which we have shown to vary with the petrologic type. From our current interpretation, however, it cannot be used to uniquely assess the petrologic type. Interestingly, we found that the BI_r position correlates with the petrologic type. Future work may demonstrate utility in identifying asteroid surfaces comprised of a high petrologic type using multiple diagnostic parameters.

We examine spectra of 13 ordinary chondrite samples —two of which are from the same meteorite—that have been subjected to high-energy laser and ion bombardment irradiation to simulate the effects brought on by space weathering (Table 1). The space weathering band parameters estimated using SAARI are shown in Figure 9a, with lines showing the same sample exposed to various irradiation doses. Unlike the fresh meteorite samples, many of these samples were not prepared into particulates, but instead left as chips for the irradiation experiment. Therefore, the BI_S of these samples are shifted somewhat to smaller, often negative, values (compare both panels of Figure 9). Changes in the spectra of irradiated samples are mostly in BI_S (up to a 40% change) and a decrease in the BI_D which exceeds 10% in some cases. The change in spectral slope and band depth averaged across all samples ($-25.5\%\ \mu m^{-1}$) is used to establish the *SWI*.

Unit bases for the space weathering coordinates are developed such that a change of one unit in the space weathered direction represents a change in spectral slope of $0.15\,\mu m^{-1}$ and one unit change in the orthogonal direction represents a change in band depth of 10%. These values for basis lengths are somewhat arbitrary but are chosen to reflect the magnitude of variations due to grain size in comparison to the changes caused by space weathering. In other words, we attempt to find a useful "measuring stick" that can be used to indicate when two asteroids that differ by $\Delta SWI \sim 1$ and $\Delta BDI \sim 1$ indicate meaningful changes. The basis coordinates are combined to form a 2×2 matrix that represents a transformation from the space weathering coordinates to the original spectral slope and band depth parameters. Inverting this matrix yields formulae for converting spectral slope and band depth to the space weathering coordinate system:

$$SWI = 5.14\ (BI_S - 0.053\ [\pm 0.084]) + 0.60\ BI_D$$

and

$$BDI = 1.96\ (BI_S - 0.053\ [\pm 0.084]) + 7.71\ BI_D,$$

where BI_D is expressed as a fraction, not a percentage. An adjustment to the BI_S is necessary in order to align the *SWI* zero point with the meteorite cluster, which is done by subtracting 0.053 from the BI_S in both equations. These equations represent a shearing and translation of the original BI_D and BI_S coordinate axes, as depicted by the grid lines in both panels of Figure 9.

Comparison to Bus-DeMeo Principal Components

Another proposed scheme for assessing the degree of space weathering uses principal components from the Bus-DeMeo asteroid taxonomy, dubbed the Space Weathering Parameter" ($\Delta\eta$) (Binzel et al., 2010, 2019). This parameter is based on the concept that the S-Sq-Q taxonomic trend is chiefly due to space weathering irradiation. In the Bus-DeMeo taxonomy, spectral slope is removed prior to calculating the principal components. Because principal components capture natural variations in spectral features among the asteroid population, compositional and grain size variations are also factors.

The Δη parameter is mostly affected by the band depth of *BI*, as stated in the original work (Binzel et al., 2010), so it is not clear to what extent this parameter accurately represents changes in space weathering. Given the latter point, we expect Δη to correlate mostly with BI_D, or the *BDI*, instead of BI_S or the *SWI*.

To test this expectation, and for a comparison to the *SWI*, we calculate Δη for the set of meteorites in our sample by calculating their PC1' and PC2' principal components in the Bus-DeMeo classification scheme. Figure 8 shows the meteorite data set, with multiple panels showing the chemical groups (panel a), petrologic types (b), and grain sizes (c). The average Δη decreases with thermal alteration of the samples: 0.341 ± 0.344 for UOCs, 0.095 ± 0.368 for type 4, -0.183 ± 0.596 for type 5, and -0.419 ± 0.529 for type 6. However, it is not immediately clear how the compositional and grain size variation affects the Δη. We also include the irradiated samples in Figure 9a, with colors indicating their chemical group. It is clear that Δη does follow the general trend shown by these samples. The number of meteorites that fall into each taxonomic class is given in Table 9, corresponding to chemical group, petrologic type and grain size. It is interesting to notice a large number of O-type meteorite spectra, which are of higher petrologic type, and that some fresh meteorites (UOCs with small grain size) are classified as S-types.

The principal components of six ordinary chondrite samples fall outside of the defined boundary for S-complex asteroids (dubbed the grand divide). All of these samples have minor *BI* and *BII* absorption features. Five of these meteorites are UOCs and two are from the same meteorite, L5 Paragould. Shock darkening has been identified as an explanation for some asteroid spectra with OC-like absorption features that fall in this region (Battle et al., 2022; Binzel et al., 2019; Kohout et al., 2020). Given that some OC meteorites fall outside of the S-complex zone, it is not immediately clear to attribute the shock darkening explanation to asteroid spectra with olivine and pyroxene absorptions that fall outside the S-complex region. Further investigation of this is beyond the scope of this work.

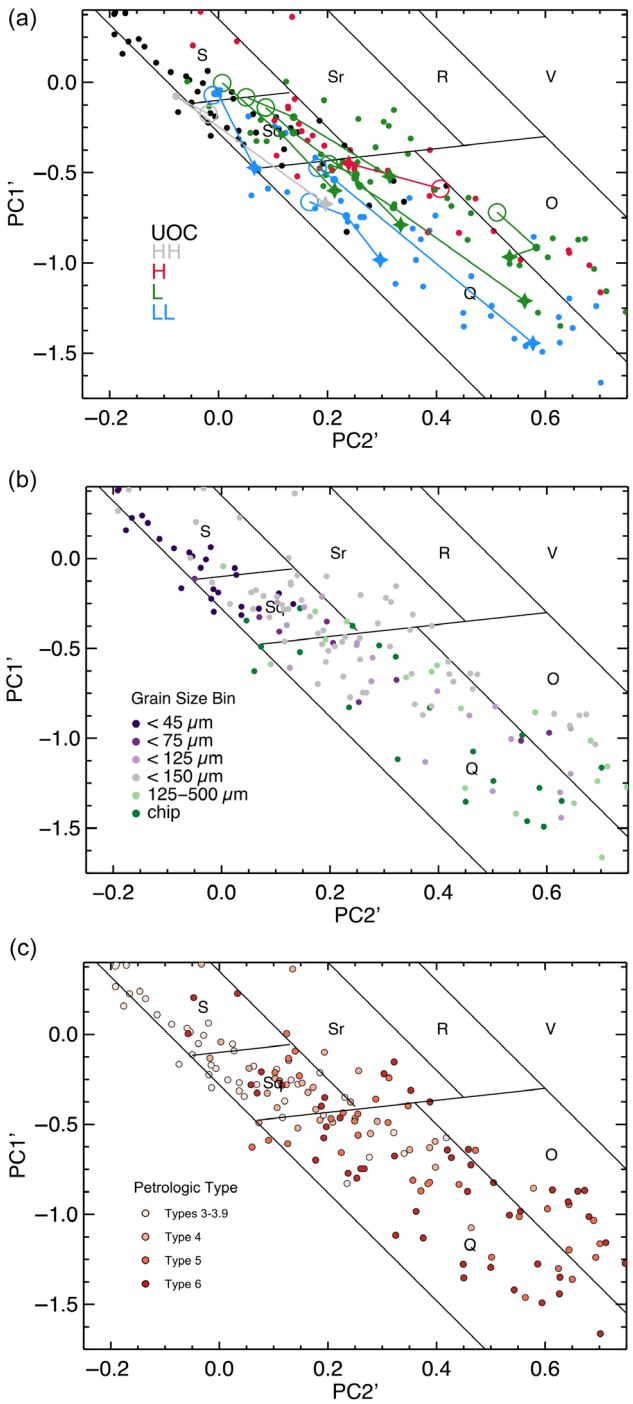

FIGURE 8. Principal components of fresh (panels a, b, c) and irradiated (panel a) ordinary chondrites. Panel (a) shows the fresh OCs colored by chemical group with the irradiated samples at different doses shown as connected lines. Panels (b and c) show only fresh meteorites colored by grain size and petrologic type according to the color schemes in Figures 4 and 5. (Color figure can be viewed at wileyonlinelibrary.com)

DISCUSSION

We designed a spectral analysis routine, SAARI, as a minimally subjective approach for the calculation of spectral band parameters. A comparison of spectral band parameter analysis techniques was outlined by Mitchell et al. (2022). They noted, in particular, the differences in the calculated band I center for that of Sanchez et al. (2015), Dunn, McCoy, et al. (2010), M4AST, and SARA. An important factor is the choice in order of polynomial fits to the reflectance data. Corrections to band parameters were suggested to account for these differences, but we find this step to be a cumbersome addition to the ever-growing list of corrections that must

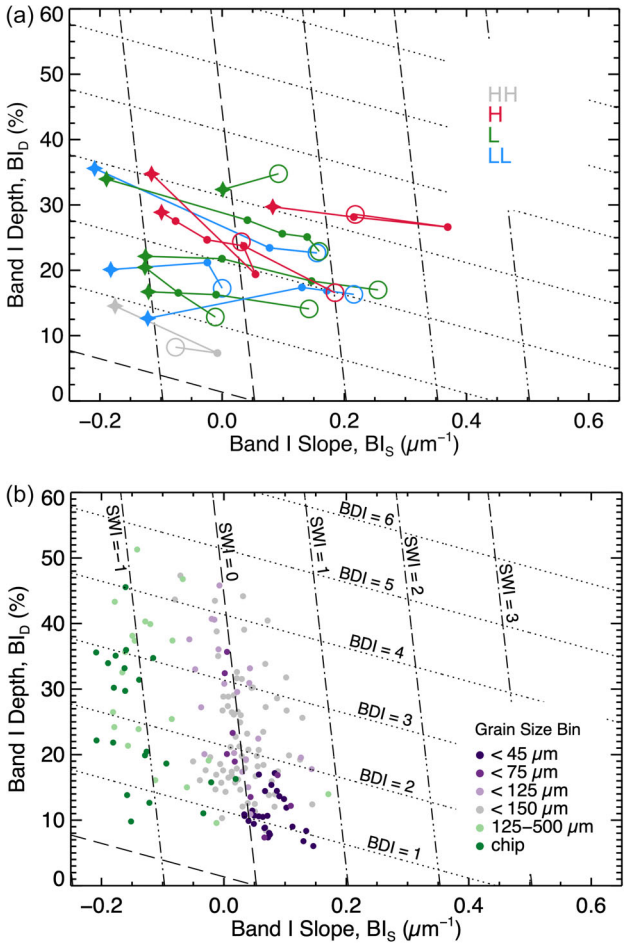

FIGURE 9. Space weathering parameters, BI_S and BI_D, of irradiated (panel a) and fresh (panel b) ordinary chondrites. Grid lines show the *SWI* (dotted) and *BDI* (dashed) coordinates. Colors of irradiated samples indicate the chemical group consistent with other figures. Lines in panel (a) connect the same meteorite sample at different irradiation doses, with stars and open circles representing the unirradiated and completely irradiated samples, respectively (see Table 1). Colors of fresh samples in panel (b) indicate the grain size bin (r chip) consistent with other figures. (Color figure can be viewed at wileyonlinelibrary.com)

be made to compare meteorite band parameters to asteroids (Reddy et al., 2015). Our choice to use a smoothing algorithm in SAARI mitigates the choices related to different polynomial fits over different wavelength windows (e.g., Mitchell et al., 2022).

One aspect that we have not chosen to pursue is to redevelop calibration equations to estimate the Fa and Fs compositions of olivine and pyroxene. McClure and Lindsay (2022) demonstrated an essential need to develop independent calibration equations for each band analysis routine. In this work, we have demonstrated how a self-consistent framework can be constructed. To avoid complications that can arise from comparing band parameters that have been calculated from using different routines, we encourage other investigators to consider this approach.

The olivine and pyroxene compositions of the UOC chondrules demonstrate a large variability, as their chondrules have not thermodynamically equilibrated fully with the surrounding matrix (Huss et al., 2006). Even though the olivine iron contents show a similar trend in relation to their corresponding equilibrated chemical group counterparts, they are more similar to one-another than those found among EOCs (Dodd et al., 1967; McSween Jr., 1992). This justifies why their spectral parameters can be treated as a distinct grouping, as shown in Figures 6 and 7, despite having varying compositions. Progressive heating in the EOCs caused the diffusion of metallic Fe, resulting in an increase of silicate FeO—depending on the oxidation conditions (highest in LL and lowest in H; Rubin & Ma, 2017)—and in the equilibration of chondrule compositions with the matrix. Low petrologic type UOCs were slightly metamorphosed in reduced conditions (Dodd et al., 1967) and with EOCs showing evidence of oxidation starting with type 4 samples (Dunn, McSween Jr., et al., 2010; McSween et al., 1991). The oxidation and thermal conditions produce olivine at the expense of pyroxene (McSween Jr. & Labotka, 1992), which is more pronounced among H chondrites and for higher temperatures (Dunn, McSween Jr., et al., 2010). This results in olivine/pyroxene variations within each chemical group that, in turn, affect band parameters to varying degrees (Table 4, Figure 5). We can see this result in our LDA that classifies spectra into both petrologic types and chemical groups (Table 8).

TABLE 9. Bus-DeMeo taxonomic classification of fresh meteorite spectra.

	Group (no UOC)			Pet. type				Grain size bin (μm)				
Tax.	H	L	LL	<4	4	5	6	<75	<125	<150	125–500	Chip
O	8	8	6	0	1	8	13	1	3	10	6	2
Q	10	22	28	0	11	19	30	4	13	24	10	15
Sq	10	7	5	20	10	5	7	3	4	19	2	2
S	5	2	1	34	3	2	3	1	0	8	1	0
Sr	3	8	0	0	4	4	3	0	0	10	0	1
L	0	0	0	5	0	0	0	0	0	1	0	0
K	0	0	0	4	0	0	0	0	0	0	0	0

We show that some band parameters such as the *BI* red-edge (BI_r) are correlated with the petrologic type. We also find that band depth variations, expressed as the *BDI*, could be used as an indicator of petrologic type. Future work can further utilize these findings to investigate petrologic type variations among the asteroid population. For example, the potential identification of a size-dependent variation of petrologic types could give insight as to the formation and evolution of planetesimals in the early solar system. The onion shell model of the ordinary chondrite parent body is a plausible explanation for the formation of various petrologic/metamorphic types seen in the meteorite record (~2/3 of L are petrologic type 6 and ~ 2/3 of H and LL are of petrologic types 5 or 6; Hutchison, 2004; Vernazza et al., 2014). Also, given the relatively low abundance of UOCs (4% among OCs; Grady, 2000; Menzies et al., 2005), we can expect to find very few asteroids with spectral properties corresponding to lower petrologic types.

A method for characterizing petrologic type of UOC-like spectra via the amount of clinopyroxene estimated from the band II position is presented by Sears et al. (2021). Our LDA classification model demonstrates how OC-like asteroids can be classified into UOC, H, L, and LL groupings using BI_C, BII_M, and *BAR*. Visual inspection of Figure 7 shows how the LDA model is able to distinguish the UOCs from EOCs, which is possible because of the inclusion of the *BII* position (see Figure 5c) in the LDA. For practical purposes, darker UOC material may be difficult to identify among asteroid spectra, as relatively brighter EOC spectra may spectrally dominate the reflected sunlight from these surfaces. The LDA results presented herein offer a method to identify UOC spectra, yet users should be cautious when applying such calibration equations to asteroid spectra that may be UOC material.

In our work, we have not attempted to redevelop calibration formulae for calculating mineral abundances and chemistries (i.e., olivine Fa and orthopyroxene Fs content). Only EOCs of a single grain size were used by Dunn, McCoy, et al. (2010) and Dunn, McSween Jr., et al. (2010) to calibrate equations for estimating the iron content in olivine (Fa#) and orthopyroxene (Fs#). Given that such diagnostic band parameters are affected by petrologic type and non-compositional factors such as grain size (Table 4), brings up doubt as to whether such formulae can be applied to asteroids with confidence that the result will be true to the purported accuracy and precision. As such, we are confident that the classification of asteroid spectra into chemical groups (and petrologic types) will yield reasonably accurate and consistent results.

We have based the *SWI* on the spectra of fresh and irradiated meteorite samples. This approach differs from other systems that use taxonomic class abundances (e.g., the ratio of Q-types to S-types) to infer space weathering mechanisms among the asteroid population (e.g., Binzel et al., 2019; DeMeo et al., 2023). The taxonomic system is based on the naturally occurring spectral variability of asteroids, which can be influenced by grain size and composition in addition to space weathering. For example, it is often presumed that Q-types always represent spectrally fresh asteroid surfaces and S-types are the space weathered counterpart. As we have pointed out in section some irradiated chips can still exhibit Q-type features (Figure 8a), as also concluded by Hasegawa et al. (2019). Therefore, we posit that the taxonomic classes can partly capture grain size variations, muddling a "pure" space weathering explanation. Interestingly, Eschrig et al. (2022) showed two different space weathering and grain size trends using principal component analyses, but these trends were shown to not completely be independent from one another. More detailed analysis, possibly combining principal components with spectral slopes, may be able to better separate space weathering and grain size effects.

The effect of space weathering on lunar regolith band parameters is distinct between the anorthositic highlands and basaltic maria (Pieters et al., 2000) and is specifically dependent on the amount of FeO in the regolith/rock (Lucey et al., 1998; Morris, 1978). Therefore, one may expect to see similar differences among OCs. We do not find any differences in space weathering trends among the different OC chemical groups, despite their differing olivine/pyroxene abundances and FeO contents. This inconclusive result could be due to the low number of irradiated samples considered herein. Interestingly, asteroids with higher spectral slope have been observed to have higher olivine content (Vernazza et al., 2009), which is consistent with higher olivine content being more sensitive to space weathering. However, this interpretation is not obvious, as the spectral slope can increase with FeO content, as just mentioned. We plan to explore the effects of Fe-rich olivine and pyroxene compositions in future work.

The spectra of irradiated meteorite samples are classified in the Bus-DeMeo asteroid taxonomy (Table 2) for which we find a large fraction of Q-types, even among the most irradiated samples. As many irradiated samples are centimeter-scale chips, this result implies that irradiated surfaces dominated by larger grains can be spectrally similar to fresh particulate surfaces, as claimed by Hasegawa et al. (2019). In the light of our interpretation of spectral slope variation of meteorite spectra, we suppose that the effect of space weathering may be overstated in the literature and a reevaluation of the relevant hypotheses and conclusions is warranted.

CONCLUSIONS

To conclude, we highlight some main points from our methods and related discussion:

- Ordinary chondrite powders comprised of larger particle sizes show a decrease in the spectral slope across the 1 μm absorption band and mimic changes due to simulated space weathering via experimental irradiation.
- Unequilibrated ordinary chondrites of lower petrologic type exhibit a trend of more attenuated absorption bands (smaller band depths). Several band parameters are also affected by the petrologic type (Table 4).
- We found that some band parameters traditionally used for mineralogical analysis of asteroids, such as the 1 μm band center and band area ratio, are dependent on the grain size of the sample.
- We demonstrate the utility of linear-discriminant analysis (LDA) as a method that can minimize non-compositional influences, such as grain size, when classifying reflectance spectra of ordinary chondrites into their compositional groups and petrologic types.
- Our space weathering index (SWI) is a simple heuristic for measuring the degree of space weathering of an asteroid spectrum and is complimentary to using Bus-DeMeo principal components.

Acknowledgments—The authors thank Thomas Burbine and Pierre Vernazza for their insightful reviews of this manuscript. E.M.M. was supported by the NASA Earth and Space Science Fellowship (NNX14AP21H). This research utilizes spectra acquired with the NASA RELAB facility at Brown University. Article open access funded by the University of Helsinki Library.

Conflict of Interest Statement—All authors declare that there is no conflict of interest (financial or otherwise) related to the work carried out in this manuscript.

Editorial Handling—Dr. A. J. Timothy Jull

Endnotes

[1] http://www.planetary.brown.edu/relab/.
[2] https://www.lpi.usra.edu/meteor/.

REFERENCES

Adams, J. B., and Filice, A. L. 1967. Spectral Reflectance 0.4 to 2.0 Microns of Silicate Rock Powders. *Journal of Geophysical Research* 72: 5705–15.

Adams, J. B., and McCord, T. B. 1971. Optical Properties of Mineral Separates, Glass, and Anorthositic Fragments from Apollo Mare Samples. *2nd Lunar and Planetary Science Conference Proceedings*, pp. 2183.

Battle, A., Reddy, V., Sanchez, J. A., Sharkey, B., Pearson, N., and Bowen, B. 2022. Physical Characterization of Near-Earth Asteroid (52768) 1998 OR2: Evidence of Shock Darkening/Impact Melt. *The Planetary Science Journal* 3: 226.

Binzel, R. P., DeMeo, F. E., Turtelboom, E. V., Bus, S. J., Tokunaga, A., Burbine, T. H., Lantz, C., et al. 2019. Compositional Distributions and Evolutionary Processes for the Near-Earth Object Population: Results from the MIT-Hawaii Near-Earth Object Spectroscopic Survey (MITHNEOS). *Icarus* 324: 41–76.

Binzel, R. P., Morbidelli, A., Merouane, S., DeMeo, F. E., Birlan, M., Vernazza, P., Thomas, C. A., Rivkin, A. S., Bus, S. J., and Tokunaga, A. T. 2010. Earth Encounters as the Origin of Fresh Surfaces on near-Earth Asteroids. *Nature* 463: 21.

Bowen, B., Reddy, V., De Florio, M., Kareta, T., Pearson, N., Furfaro, R., Sharkey, B., et al. 2023. Grain Size Effects on Visible and Near-Infrared (0.35–2.5 μm) Laboratory Spectra of Ordinary Chondrite and HED Meteorites. *The Planetary Science Journal* 4: 3.

Brunetto, R., Loeffler, M. J., Nesvorn'y, D., Sasaki, S., and Strazzulla, G. 2015. Asteroid Surface Alteration by Space Weathering Processes. In *Asteroids IV*, edited by P. Michel, F. E. DeMeo, and W. F. Bottke, Jr., 597–616. Tucson, AZ: University of Arizona Press.

Burns, R. G. 1993. Mineralogical Applications of Crystal Field Theory. In *Cambridge Topics in Mineral Physics and Chemistry*, 2nd ed, edited by M. F. Hochella, Jr., R. C. Liebermann, and A. Putnis. Cambridge, UK: Cambridge University Press.

Cappellari, M., McDermid, R. M., Alatalo, K., Blitz, L., Bois, M., Bournaud, F., Bureau, M., et al. 2013. The ATLAS3D Project – XX. Mass-Size and Mass-σ Distributions of Early-Type Galaxies: Bulge Fraction Drives Kinematics, Mass-to-Light Ratio, Molecular Gas Fraction and Stellar Initial Mass Function. *Monthly Notices of the Royal Astronomical Society* 432: 1862–93.

Chapman, C. R. 2004. Space Weathering of Asteroid Surfaces. *Annual Review of Earth and Planetary Sciences* 32: 539–567.

Cleveland, W. S. (1979). Robust locally weighted regression and smoothing scatterplots. *Journal of the American Statistical Association*, 74(368), 829–836. https://doi.org/10.1080/01621459.1979.10481038

Cloutis, E. A., Gaffey, M. J., Jackowski, T. L., and Reed, K. L. 1986. Calibrations of Phase Abundance, Composition, and Particle Size Distribution for Olivine-Orthopyroxene Mixtures from Reflectance Spectra. *Journal of Geophysical Research* 91: 11641–53.

Conel, J. E., and Nash, D. B. 1970. Apollo 11 Rocks Spectral Reflectance and Albedo before/after Proton Irradiation and Vitrification, Investigating Color Differences for Lunar Surface Dark and Bright Areas. *3rd Apollo 11 Lunar Science Conference*, pp. 2013–2023.

Delbo, M., Dell'Oro, A., Harris, A. W., Mottola, S., and Mueller, M. 2007. Thermal Inertia of Near-Earth Asteroids and Implications for the Magnitude of the Yarkovsky Effect. *Icarus* 190: 236–249.

Delbo, M., and Tanga, P. 2009. Thermal Inertia of Main Belt Asteroids Smaller than 100 km from IRAS Data. *Planetary and Space Science* 57: 259–265.

DeMeo, F. E., Marsset, M., Polishook, D., Burt, B. J., Binzel, R. P., Hasegawa, S., Granvik, M., et al. 2023. Isolating the Mechanisms for Asteroid Surface Refreshing. *Icarus* 389: 115264.

Dodd, R. T., VanSchmus, W. R., and Koffman, D. M. 1967. A Survey of the Unequilibrated Ordinary Chondrites. *Geochimica et Cosmochimica Acta* 31: 921–934.

Duffard, R., Lazzaro, D., & de León, J. (2005). Revisiting spectral parameters of silicate-bearing meteorites. *Meteoritics & Planetary Science*, 40(3), 445–459. https://doi.org/10.1111/j.1945-5100.2005.tb00393.x

Dunn, T. L., McCoy, T. J., Sunshine, J. M., and McSween, H. Y., Jr. 2010. A Coordinated Spectral, Mineralogical, and Compositional Study of Ordinary Chondrites. *Icarus* 208: 789–797.

Dunn, T. L., McSween, H. Y., Jr., McCoy, T. J., and Cressey, G. 2010. Analysis of Ordinary Chondrites Using Powder X-Ray Diffraction: 2. Applications to Ordinary Chondrite Parent-Body Processes. *Meteoritics & Planetary Science* 45, 1: 135–156.

Eschrig, J., Bonal, L., Mahlke, M., Carry, B., Beck, P., and Gattacceca, J. 2022. Investigating S-Type Asteroid Surfaces through Reflectance Spectra of Ordinary Chondrites. *Icarus* 381: 115012.

Fei, Y., Bertka, C. M., and Finger, L. W. 1997. High-Pressure Iron-Sulfur Compound, Fe_3S_2, and Melting Relations in the Fe-FeS System. *Science* 275: 1621–23.

Fisher, R. A. 1919. XV.—The Correlation between Relatives on the Supposition of Mendelian Inheritance. *Transactions of the Royal Society of Edinburgh* 52: 399–433.

Fisher, R. A. 1936. The Use of Multiple Measurements in Taxonomic Problems. *Annals of Eugenics* 7: 179–188.

Gaffey, M. J. 2010. Space Weathering and the Interpretation of Asteroid Reflectance Spectra.

Gaffey, M. J., Bell, J. F., Brown, R. H., Burbine, T. H., Piatek, J. L., Reed, K. L., and Chaky, D. A. 1993. Mineralogical Variations within the S-Type Asteroid Class. *Icarus* 106: 573–602.

Gaffey, M. J., Burbine, T. H., and Binzel, R. P. 1993. Asteroid Spectroscopy: Progress and Perspectives. *Meteoritics* 28: 161–187.

Gaffey, M. J., Cloutis, E., Kelley, M. S., and Reed, K. 2002. Mineralogy of Asteroids. In *Asteroids III*, edited by W. F. Bottke, Jr., A. Cellino, P. Paolicchi, and R. P. Binzel, 183–204. Tucson, AZ: University of Arizona Press.

Gaffey, M. J., Reddy, V., Fieber-Beyer, S., and Cloutis, E. 2015. Asteroid (354) Eleonora: Plucking an Odd Duck. *Icarus* 250: 623–638.

Ghosh, A., and McSween, H. Y., Jr. 1998. A Thermal Model for the Differentiation of Asteroid 4 Vesta, Based on Radiogenic Heating. *Icarus* 134: 187–206.

Gietzen, K. M., Lacy, C. H. S., Ostrowski, D. R., and Sears, D. W. G. 2012. IRTF Observations of S-Complex and Other Asteroids: Implications for Surface Compositions, the Presence of Clinopyroxenes, and their Relationship to Meteorites. *Meteoritics & Planetary Science* 47: 1789–1808.

Grady, M. 2000. *Catalogue of Meteorites*, 2nd ed. Cambridge: Cambridge University Press. 689.

Gundlach, B., and Blum, J. 2013. A New Method to Determine the Grain Size of Planetary Regolith. *Icarus* 223: 479–492.

Hapke, B. (2001). Space weathering from Mercury to the asteroid belt. *Journal of Geophysical Research: Planets*, 106 (E5), 10039–73. https://doi.org/10.1029/2000je001338

Harvey, R. 2003. The Origin and Significance of Antarctic Meteorites. *Chemie der Erde* 63: 93–147.

Hasegawa, S., Hiroi, T., Ohtsuka, K., Ishiguro, M., Kuroda, D., Ito, T., and Sasaki, S. 2019. Q-Type Asteroids: Possibility of Non-Fresh Weathered Surfaces. *Proceedings of the Astronomical Society of Japan* 71: 103.

Huss, G. R., Rubin, A. E., and Grossman, J. N. 2006. Thermal Metamorphism in Chondrites. In *Meteorites and the Early Solar System II*, edited by D. S. Lauretta, and H. Y. McSween, Jr., vol. 943, 567–586. Tucson, AZ: University of Arizona Press.

Hutchison, R. 2004. *Meteorites: A Petrologic, Chemical and Isotopic Synthesis*. Cambridge: Cambridge University Press.

Kanuchova, Z., Brunetto, R., Fulvio, D., & Strazzulla, G. (2015). Near-ultraviolet bluing after space weathering of silicates and meteorites. *Icarus*, 258, 289–296. https://doi.org/10.1016/j.icarus.2015.06.030

Kohout, T., Penttilä, A., Mann, P., Cloutis, E., Čuda, J., Filip, J., Malina, O., et al. 2020. Distinguishing between Shock-Darkening and Space-Weathering Trends in Ordinary Chondrite Reflectance Spectra. *The Planetary Science Journal* 1: 37.

Lindsay, S. S., Marchis, F., Emery, J. P., Enriquez, J. E., and Assafin, M. 2015. Classification and Mineralogy of Multiple Asteroid Systems from Visible and Near-Infrared Spectral Data. *Icarus* 247: 53–70.

Lord, S. D. 1992. *A New Software Tool for Computing Earth's Atmospheric Transmission of near- and Far-Infrared Radiation*. Technical Report 103957. NASA Technical Memorandum. Moffett Field, CA: Ames Research Center.

Lucas, M. P., Emery, J. P., Hiroi, T., and McSween, H. Y. 2019. Spectral Properties and Mineral Compositions of Acapulcoite-Lodranite Clan Meteorites: Establishing S-Type Asteroid-Meteorite Connections. *Meteoritics & Planetary Science* 54: 157–180.

Lucey, P. G., Blewett, D. T., and Hawk, B. R. 1998. Mapping the FeO and TiO_2 Contentof the Lunar Surface with Multispectral Imagery. *Journal of Geophysical Research* 103(E2): 3679–99.

MacLennan, E. M. 2019. *Asteroid Regolith Weathering: A Large-Scale Observational Investigation*. Ph.D. Thesis. Knoxville, TN: University of Tennessee.

MacLennan, E. M., and Emery, J. P. 2022. Thermophysical Investigation of Asteroid Surfaces. II. Factors Influencing Grain Size. *The Planetary Science Journal* 3: 47.

McClure, L. T., and Lindsay, S. S. 2022. A Contemporary View of the Ordinary Chondrite Boot I: Band Parameter Analysis Dependency. *Icarus* 379: 114907.

McCord, T. B., and Johnson, T. V. 1970. Lunar Spectral Reflectivity (0.3 to 2.5 microns) and Implications for Remote Mineralogical Analysis. *Science* 169: 855–58.

McSween, H. Y., Jr. 1992. Redox Effects in Ordinary Chondrites and Implications for Asteroid Spectroscopy. *Icarus* 95: 239–243.

McSween, H. Y., Bennett, M. E., & Jarosewich, E. (1991). The mineralogy of ordinary chondrites and implications for asteroid spectrophotometry. *Icarus*, 90(1), 107–116. https://doi.org/10.1016/0019-1035(91)90072-2

McSween, H. Y., Jr., and Labotka, T. 1992. Oxidation during Metamorphism of the Ordinary Chondrites. *Geochimica et Cosmochimica Acta* 57: 1105–14.

Menzies, O. N., Bland, P. A., Berry, F. J., and Cressey, G. 2005. A Mössbauer Spectroscopy and X-Ray Diffraction Study of Ordinary Chondrites: Quantification of Modal

Mineralogy and Implications for Redox Conditions during Metamorphism. *Meteoritics & Planetary Science* 40: 1023–42.

Mitchell, A. M., Reddy, V., Sharkey, B. N. L., Sanchez, J. A., Burbine, T. H., Le Corre, L., and Thomas, C. A. 2022. Constraining Ordinary Chondrite Composition Via Near-Infrared Spectroscopy. *Icarus* 336: 113426.

Miyamoto, M., Fujii, N., and Takeda, H. 1981. Ordinary Chondrite Parent Body: An Internal Heating Model. *Proceedings of the Lunar Planetary Science Conference* 12B: 1145–52.

Moroz, L. V., Fisenko, A. V., Semjonova, L. F., Pieters, C. M., & Korotaeva, N. N. (1996). Optical effects of regolith processes on S-asteroids as simulated by laser shots on ordinary chondrite and other mafic materials. *Icarus*, 122 (2), 366–382. https://doi.org/10.1006/icar.1996.0130

Morris, R. V. 1978. The Surface Exposure (Mature) of Lunar Soils: Some Concept and Is/Feo Compilation. *Proceedings of the Lunar and Planetary Science Conference* IX, pp. 2287–2297.

Pieters, C. M., and Hiroi, T. 2004. RELAB (Reflectance Experiment Laboratory): A NASA Multiuser Spectroscopy Facility. In *Lunar and Planetary Science Conference XXXV*, abstract #1720.

Pieters, C. M., and Noble, S. K. 2016. Space Weathering on Airless Bodies. *Journal of Geophysical Research: Planets* 121: 1865–84.

Pieters, C. M., Taylor, L. A., Noble, S. K., Keller, L. P., Watson, B., Morris, R. V., Allen, C. C., McKay, D. S., and Wentworth, S. 2000. Space Weathering on Airless Bodies: Resolving a Mystery with Lunar Samples. *Meteoritics & Space Science* 35: 1101–7.

Popescu, M., Birlan, M., and Nedelcu, D. A. 2012. Modeling of Asteroid Spectra – M4AST. *Astronomy & Astrophysics* 544, A130 (10 pp).

Reddy, V., Dunn, T. L., Thomas, C. A., Moskovitz, N. A., and Burbine, T. H. 2015. Mineralogy and Surface Composition of Asteroids. In *Asteroids IV*, edited by P. Michel, F. E. DeMeo, and W. F. Bottke, Jr., 43–63. Tucson, AZ: University of Arizona Press.

Rubin, A. E. (1990). Kamacite and olivine in ordinary chondrites: Intergroup and intragroup relationships. *Geochimica et Cosmochimica Acta*, 54(5), 1217–32. https://doi.org/10.1016/0016-7037(90)90148-e

Rubin, A. E., and Ma, C. 2017. Meteoritic Minerals and their Origins. *Chemie der Erde* 77: 325–385.

Sanchez, J. A., Reddy, V., Dykhuis, M., Lindsay, S., & Corre, L. L. (2015). Composition of potentially hazardous asteroid (214869) 2007 PA8: An H chondrite from the outer asteroid belt. *The Astrophysical Journal*, 808(1), 93. https://doi.org/10.1088/0004-637x/808/1/93

Sears, D., Ostrowski, D., Smith, H., Sissay, A., and Trivedi, M. 2021. A New Method for Determining the Petrologic Type of Unequilibrated Ordinary Chondrites that can be Applied to Asteroids. *Icarus* 363: 114442.

Strazzulla, G., Dotto, E., Binzel, R., Brunetto, R., Barucci, M., Blanco, A., and Orofino, V. 2005. Spectral Alteration of the Meteorite Epinal (H5) Induced by Heavy Ion Irradiation: A Simulation of Space Weathering Effects on Near-Earth Asteroids. *Icarus* 174: 31–35.

Taylor, L. A., Pieters, C. M., Keller, L. P., Morris, R. V., McKay, D. S., Patchen, A., and Wentworth, S. 2001. The Effects of Space Weathering on Apollo 17 Mare Soils: Petrographic and Chemical Characterization. *Meteoritics & Planetary Science* 36: 285–89.

Vernazza, P., Binzel, R. P., Rossi, A., Fulchignoni, M., & Birlan, M. (2009). Solar wind as the origin of rapid reddening of asteroid surfaces. *Nature*, 458(7241), 993–95. https://doi.org/10.1038/nature07956

Vernazza, P., Marsset, M., Beck, P., Binzel, R. P., Birlan, M., Cloutis, E. A., DeMeo, F. E., Dumas, C., & Hiroi, T. (2016). Compositional homogeneity of CM parent bodies. *The Astronomical Journal*, 152(3), 54. https://doi.org/10.3847/0004-6256/152/3/54

Vernazza, P., Zanda, B., Binzel, R. P., Hiroi, T., DeMeo, F. E., Birlan, M., Hewins, R., Ricci, L., Barge, P., and Lockhart, M. 2014. Multiple and Fast: The Accretion of Ordinary Chondrite Parent Bodies. *Astrophysical Journal* 791: 120.